Chemical Engineering Journal 447 (2022) 137468

Contents lists available at ScienceDirect

Chemical Engineering Journal

journal homepage: www.elsevier.com/locate/cej

Review

Plant-derived hard carbon as anode for sodium-ion batteries: A comprehensive review to guide interdisciplinary research

Darío Alvira *, Daniel Antorán, Joan J. Manyà

Aragón Institute of Engineering Research (I3A), Thermochemical Processes Group, University of Zaragoza, Escuela Politécnica Superior, 22071 Huesca, Spain

ARTICLE INFO

Keywords:
Sodium-ion battery
Hard carbon
Plant-derived biomass
Mechanism of Na-ion storage
Electrochemical performance

ABSTRACT

Sodium-ion batteries (SIBs) are one of the most promising candidates to replace lithium-ion batteries (LIBs) in grid-scale energy storage applications. SIBs technology is still in an early development stage and new feasible and low-cost active materials are required. The design of high-performance anodes and the fully understanding of the sodium storage mechanisms are the main bottleneck to overcome. Hard carbons (HCs) are extensively studied as anode material since sodium ions can be intercalated in pseudographitic domains and reversibly adsorbed in surface edges, defects and nanopores. This review aims at providing a comprehensive overview of the current state of knowledge of plant-derived HC anodes in SIBs, which can be helpful for researchers from different backgrounds working in the field. Working principles of SIBs are summarized, together with a detailed description of the Na-ion storage mechanisms in hard carbon anodes proposed to date. Finally, an exhaustive literature review on the performance of plant-derived HCs in SIBs is presented, with special focus on the synthesis pathways (including activation and/or doping treatments).

1. Introduction

Global warming and shortage of natural resources, together with a progressive rise in energy demand, poses a challenge for energy production, storage, and distribution. Despite the reduction in global CO_2 emissions due to the COVID-19 pandemic, atmospheric carbon dioxide concentration reached a record peak of 419 parts per million in May 2021 [1], a 50% increase above pre-industrial levels [2]. Since fossil fuels still play a key role in the current energy scenario, development of renewable, efficient, and profitable energy systems is a crucial challenge for today. All the same, using the electricity generated from intermittent renewable sources (e.g., wind and solar energy) implies the implementation of sustainable and low-cost energy storage systems to deliver current to the grid when needed [3].

Lithium-ion batteries (LIBs) are the main rechargeable batteries since their commercialization in the 90 s. However, demand and extraction of lithium have experienced a significant rise over the last years owing to the widespread usage of portable electronics and the global population growth. Moreover, a larger increase is expected due to the electric vehicle market expansion and the growing implementation of stationary grid energy storage systems [4]. Considering this scenario, a global supply shortage and a price increment can be anticipated since lithium is not widely distributed in the Earth's crust and resources are concentrated in specific regions. Almost 60% of global lithium reserves are found in lithium brines deposits located in South America, especially in Chile, Bolivia, and Argentina, while the main ore deposits as spodumene mineral are located in Australia [5]. In addition, the basic LIB components cobalt and natural graphite are also produced in some specific regions; currently, 59% of cobalt and 69% of natural graphite are extracted in Congo DR and China, respectively. The EU expects that lithium and cobalt requirements in 2030 will be 60 and 15 times higher compared to the present supply. In view of supply risk issues, lithium, cobalt, and natural graphite were included in the European 2020 critical raw materials list [6]. Consequently, electrochemical energy storage devices based on cheaper and more earth abundant elements need to be developed and implemented in the midterm in order to decrease lithium and associated materials dependence.

Sodium-ion batteries (SIBs) are one of the most promising candidates since sodium and lithium have similar physical and chemical properties (see Table 1). Both elements are neighbors in the alkali metals group and both have one loosely bound electron in their outer shell, thereby facilitating the formation of cations Li^+ and Na^+ [7]. Moreover, they have similar standard electrode potentials: –2.71 V vs SHE for Na^+/Na and –3.04 V vs SHE for Li^+/Li. On the other hand, sodium is cheaper,

* Corresponding author.
E-mail address: dalvira@unizar.es (D. Alvira).

https://doi.org/10.1016/j.cej.2022.137468
Received 14 March 2022; Received in revised form 20 May 2022; Accepted 9 June 2022
Available online 13 June 2022

Table 1
Comparison of selected properties of Li and Na [7,8,10].

	Li	Na
Abundance in the Earth's crust (wt. %)	0.0017	2.36
Atomic number	3	11
Atomic weight (g mol^{-1})	6.941	22.99
Melting point (°C)	180.54	97.72
Ionic radius (6-coordinate) (nm)	0.076	0.102
Redox potential vs. SHE (V)	–3.04	–2.71
Electronic configuration	$[He]2s^1$	$[Ne]3s^1$
Ionization energy (kJ mol^{-1})	520.2	495.8

much more abundant than lithium in earth's crust, and is widely dispersed around the planet [8]. Unfortunately, the lower energy density of SIBs hinders its implementation in some sectors where space is a limiting factor (e.g., mobile devices and the vehicle transportation sector); but allows SIBs to be used in massive storage applications (e.g., grid energy storage) where energy density is not a crucial factor [9].

SIBs research started in the early 1980s [11], but decreased substantially after the successful commercialization of LIBs in 1991 [12]. SIBs were found to have worse specific capacity, minor energy density, and lower rate and cycling performance. Compared with lithium, sodium is larger, heavier, and has a higher standard potential, therefore SIBs have lower capacity and smaller range of redox potential. In the past decade, however, interest in sodium batteries remerged driven by concerns about LIB resources availability. The discovery of Na^+ intercalation in hard carbon (HC) by Stevens and Dahn [13] in 2000 supposed a turning point in SIBs horizon. Reversible sodium capacity of 300 mA h g^{-1} was found, close to that for lithium insertion in graphite (372 mA h g^{-1}), which laid the groundwork for the current SIBs research. Fig. 1 shows the growing interest in SIBs and how "hard carbon" research follows the same trend.

In recent years, few SIBs start-ups and spin-offs have appeared on the market revealing the upward trend of this new technology. Nevertheless, SIBs technology is still in an early development stage and new active materials and electrolytes need to be investigated to further increase the attractiveness of this technology in terms of cost and performance. Selection and design of high-performance electrodes is the main challenge for SIBs development. More in detail, the performance of the anode is the bottleneck since it determines the rate of discharge and plays a critical role in the overall coulombic efficiency. Graphite is commonly used as anode material in LIBs thanks to its reversible lithium de/intercalation. Lithiated graphite (LiC_6) exhibits low operation voltage, low cost, and non-toxicity [14]. Unfortunately, Na ions cannot be intercalated into the graphite host due to thermodynamical issues and, hence, other anode materials have to be proposed.

Among carbonaceous materials, hard carbons (HCs) appear as the most promising candidates to be used in the anode, because they provide more defects and active sites to store sodium ions. Hard carbons are mainly produced from the pyrolysis of biomass or synthetic organics and its non-graphitability is due to the high oxygen and disordered structure of such precursors. HCs preserve disordered structures together with randomly oriented pseudographitic domains, which have larger interlayer spacing than graphitic carbons, allowing Na^+ accommodation. They also contain micro and mesopores and some remaining heteroatoms (N, S, P, B, etc.), that provide more sodium storage sites and pathways for faster Na^+ transport. Plant-derived hard carbons are especially promising candidates from both economic and sustainability points of view [15]. The produced carbons retain the plant tissue microstructure, which facilitates the electrolyte penetration and Na^+ diffusion. Lignocellulosic wastes can also be selected as low cost material precursors, as an interesting approach to manage an agricultural residue and simultaneously mitigate CO_2 emissions through carbonization processes.

In order to obtain suitable anode materials for SIBs, relevant properties of plant-derived hard carbons —such as the interlayer spacing, pore structure, and number of defects and heteroatoms— need to be tuned. However, in-depth knowledge of Na^+ storage mechanisms (still in discussion) is required to design a successful strategy toward the production of engineered HCs. This review aims at providing an overview of the current state of knowledge and development of carbon-based anodes in SIBs.

2. Working principle and basic considerations of SIBs

A battery can be defined as a power source that produces direct current (DC) by converting chemical energy into electrical energy [16]. It is composed of one or more electrochemical cells that connected in parallel or in series provide the desired voltage and current levels. Each cell contains a positive and a negative electrode, whose electrochemical role changes between anode (oxidation) and cathode (reduction) depending on the current direction. Nevertheless, the positive electrode is usually designed as the cathode and the negative electrode as the anode. In a SIB cell both electrodes are connected via an electrolyte and a porous separator, which blocks the flow of electrons inside the battery but allowing Na ions to flow though the cell.

The working principle of SIBs is represented in Fig. 2 and is equivalent to the "*rocking chair*" concept in LIBs. Reactions occur in a closed system, and for every electron generated in an electrode oxidation, other electron is consumed in the reduction reaction happened on the opposite electrode. During battery charging (red arrows in Fig. 2), electrons provided by the oxidation of the positive electrode travel across the

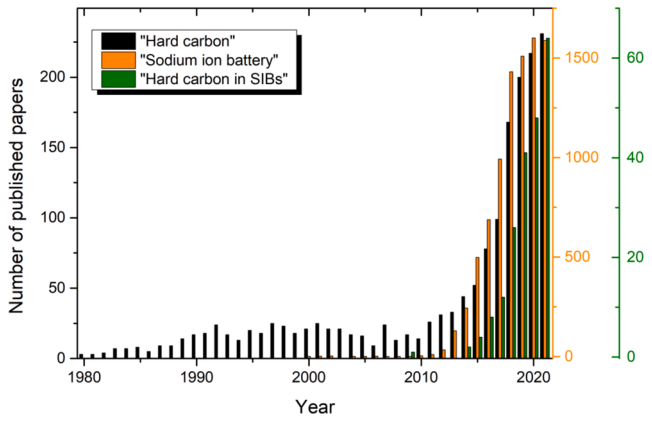

Fig. 1. Number of published articles and reviews for "hard carbon", "sodium ion battery", and "hard carbon in SIBs". Source: Scopus.

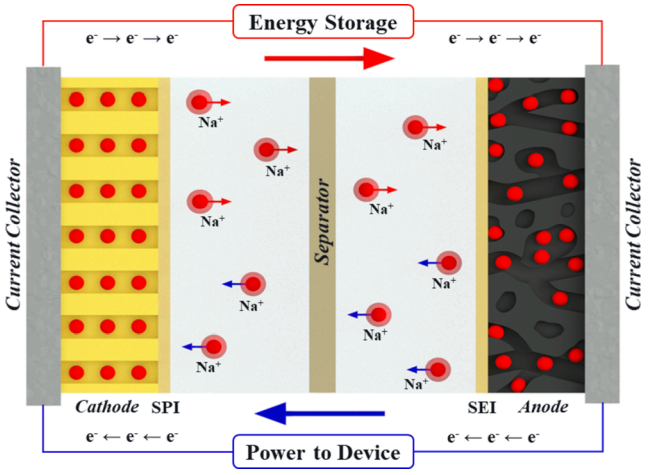

Fig. 2. Working principle of sodium ion batteries. Source: authors' own creation.

external circuit towards the anode. In order to maintain charge neutrality, Na ions go through the electrolyte and get stored in the anode. During battery discharging (blue arrows in Fig. 2), the reverse process takes place when oxidation of the anode delivers Na ions towards the cathode and the electrons travel through the external circuit providing current to external devices.

A passivation film termed as solid electrolyte interphase (SEI) is formed on the hard carbon anode surface due to the reduction of the electrolyte during the course of the first charge. Likewise, a surface layer named solid permeable interface (SPI)[1] is formed on the cathode surface due to the oxidation of the electrolyte. Both layers block electron transport while allowing the passage of the alkaline ions as pure cationic conductors, preventing further electrolyte degradation and protecting the electrodes during cycling [17,18]. However, excessive growth of the SEI in the first cycle causes severe sodium ion trapping and large capacity loss. Although the battery can deliver high enough reversible capacities after a number of cycles, larger amount of cathode mass would be required to compensate the immobilized sodium in the SEI, leading to higher volume requirements and penalties in energy density.

2.1. Hard carbon electrodes

Graphite does not work as anode in SIBs and the common argument is that sodium is too large to be intercalated into graphite layers. This statement is not convincing since, for instance, bigger K^+ ions (0.138 nm of radius) can intercalate into graphite [19,20], forming KC_8 with a theoretical capacity of 279 mA h g^{-1} [21], while lithium can be hosted as LiC_6 with a theorical capacity of 372 mA h g^{-1} [14]. Nevertheless, graphite shows very little capacity for sodium stored as NaC_{186} [22] or NaC_{64} [23]: exhibited 12 and 35 mA h g^{-1}, respectively [24].

Low formation of Na-intercalated graphite was justified since Na–C bond is very soft and there are not enough energetic forces to promote Na-ion intercalation [25]. Lenchuk et al. [26] applied density functional theory (DFT) calculations and found sodium graphite intercalation compounds (Na-GICs) thermodynamically unstable. The high capacity for Li–GICs was attributed to an additional covalent contribution that enhances the mainly ionic bonding and van der Waals interactions. Thus, inasmuch as graphite cannot be used as negative electrode, other materials need to be studied.

Insertion —or intercalation— electrodes store Na ions inside their crystal structure without disturbing their three-dimensional framework. The amount of intercalated sodium is determined by the thermodynamic equilibrium at the electrode/electrolyte interface and specific capacities higher than 400 mA h g^{-1} are seldom reached. Titanium dioxide (TiO_2) [27] and TiO_2/C nanofibers [28] are being taking into consideration, while carbonaceous materials are the most studied electrode candidates for SIBs because of its chemical and thermal stability. Carbon materials are generally classified into two main categories, graphitizable and non-graphitizable [29]. Graphitizable or soft carbons can be transformed into graphite after heat treatments over 2000 °C, while non-graphitizable or hard carbons keep its disordered structure and never get graphitized, even at 3000 °C (see Fig. 3). Nature of the raw material is strongly related to the produced carbon graphitability. Generally, gas or liquid-phase carbonization of aromatic precursors (e.g., petroleum pitch and coal tar pitch) generate non-porous soft carbon materials. On the other hand, pyrolytic products from biomass, with less aromatic structures, result in porous and amorphous hard carbons [29,30], suitable for use in SIBs.

Besides intercalation anodes, alloy- and conversion-based electrodes are being studied for SIBs. The former are based on the sodium alloying and dealloying reaction with some elements to form Na-M intermetallic binary compounds (e.g., Sn [31], Sb [32], and P [33]). Since a single atom can alloy with multiple Na ions, these anodes can provide high capacities up to 2000 mA h g^{-1}. Conversion reaction electrodes, as metal oxides [34], sulfides [35], and, selenides [36], also deliver high specific capacities up to 1800 mA h g^{-1} according to the following overall reaction:

$$M_aX_b + (bc)Na \rightleftarrows aM + bNa_cX \quad (1)$$

where M is a transition metal and X a non-metal. However, both alloy and conversion anodes suffer from large volume expansion upon cycling, giving rise to structural instability and irreversible capacity losses [37,38]. This fact explains why insertion electrodes, and especially hard carbons (which have additional benefits in terms of sustainability) became the most promising and studied materials for SIBs anodes [39].

Despite the fact that suitable HC-based electrodes were produced and successfully tested, a detailed understanding of the phenomena occurring around the negative SIB electrode is still missing. Until now, discrepant observations have been made by researchers, boosted by heterogeneity in terms of hard carbon precursors, structure, and chemical composition, together with the use of different characterization techniques. The lack of consensus on the mechanisms involving the negative electrode hinders a systematic research to develop optimum HCs for electrochemical energy storage purposes. Therefore, in-depth knowledge of the sodium storage mechanism, ion transfer process, and SEI nature must be achieved to develop competitive sodium ion batteries.

2.2. Mechanism of Na-ion storage in hard carbon anodes

While lithium insertion into graphite has been studied extensively, the sodium reversible storage mechanism in hard carbons is still unclear and controversial. Stevens et al. [40] defined the HC structure according to the “house of cards” model, containing graphite-like microcrystallites and amorphous regions. Hard carbon is non-graphitizable, presents a disordered structure, and contains abundant active sites as defects, edges, and functional groups. As a result, sodium storage is a more complex process than the lithium insertion/desertion in graphite. Three different sodium storage behaviors have been reported for HCs in the literature: (i) intercalation between graphite layers, (ii) adsorption on the surface edges and defects, and (iii) nanopore filling.

Galvanostatic charge–discharge (GCD) profiles of HC-based electrodes typically show two regions determined by the sodium storage processes: a high-potential sloping region and a plateau at potentials below 0.10 V (see Fig. 4). Unfortunately, there is still no consensus about what storage behavior occurs in each voltage region. Six models have been proposed so far to explain the mechanism behind Na^+ storage: (i) insertion-filling model, (ii) adsorption-insertion model, (iii) three stage model, (iv) four stage model, (v) extended adsorption-insertion model, and (vi) adsorption-filling model.

i) Insertion-filling model. The first sodium storage mechanism, known as insertion-filling mechanism, was proposed by Dahn et al. [13]. Glucose was pyrolyzed at 1000 and 1150 °C and the resulting carbon was considered according to the “house of cards” structure model. Random stacking generates small regions with groups of two or three graphene sheets, approximately parallel each other, as well as nanoscale porosity regions. Dahn et al. attributed the sloping potential profile to the insertion of sodium between parallel or nearly parallel layers and the low-potential plateau to the metal insertion into the nanovoids. In 2017, Dahbi et al. [41] corroborated this model by using X-ray diffraction (XRD) and pore size distribution in the sodiation of argan shell-derived HC. They found a direct relationship between the slope region (from 1.2 to 0.15 V) and the graphene layer spacing (d_{002}), in accordance with the Na^+ intercalation. They also found a positive linear relationship between the platform capacity (from 0.15 to 0.00 V) and the average micropore size, calculated by the Barrett–Joyner–Halenda (BJH)

[1] Some authors use the term *solid electrolyte interphase (SEI)* for both anode and cathode surface interphases.

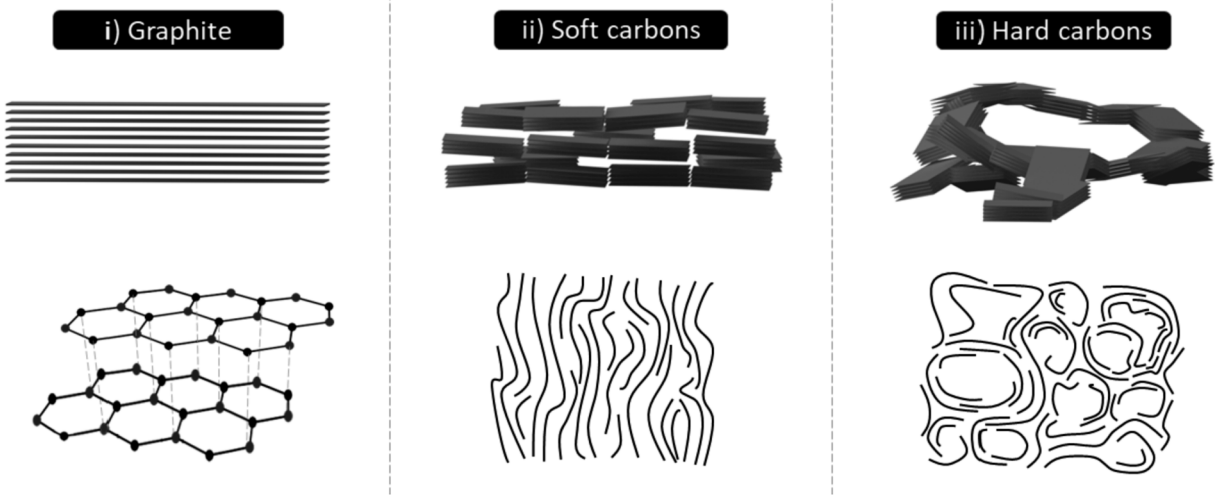

Fig. 3. Structure of graphite, soft carbons, and hard carbons.

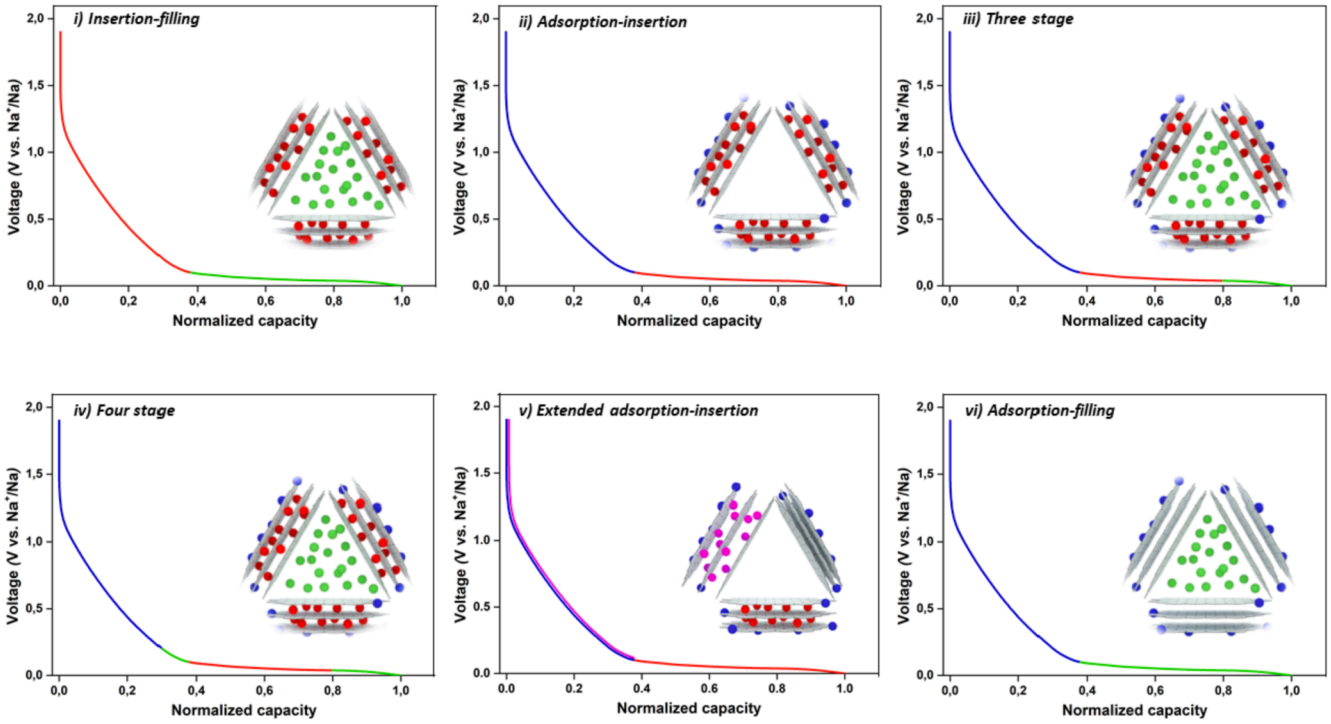

Fig. 4. Sodium storage mechanism models in SIBs. Source: authors' own creation.

method.

ii) Adsorption-insertion model. Proposed by Cao et al. [42] in 2012 from experimental results obtained for a hollow polyaniline nanowire-derived HC, this model assumes that low potential plateau below 0.1 V corresponds to Na insertion/desertion between the carbon layers, while the sloping region relates to the sodium ion adsorption on the surface. Moreover, by means of theoretical simulations they found a critical minimum spacing of 0.37 nm between the graphitic layers (with an energy barrier of 0.053 eV) to facilitate Na-ion insertion. In 2013, Ding et al. [43] supported this model and concluded that intercalation was the main storage mechanism of the plateau region when they used peat moss-derived HC. By using ex situ XRD at different state of charge, they observed a reversible inter-graphene spacing due to Na intercalation. When the HC carbonized at 1400 °C was sodiated from 0.1 to 0.001 V, the d_{002} interlayer spacing expanded from 0.396 to 0.416 nm. Zhang et al. [44] further investigated this mechanism for lotus stems-derived HC and corroborated the Na^+ adsorption in defect sites as the sloping region storage process. Moreover, they attributed the platform region to the Na^+ deposition in closed pores in addition to the Na metal insertion between the graphite layers.

iii) Three stage model. In line with the adsorption-insertion model, Bommier et al. [45] also detected the reversible interlayer expansion of glucose-derived HC by three different techniques: ex-situ XRD, Raman spectroscopy and neutron diffraction measurements. Moreover, neutron pair distribution function (PDF) analysis provided defect storage sites concentration associated with the sloping region. However, using galvanostatic intermittent titration (GITT), they found an increase in the sodium diffusion coefficient values at the end of the plateau region, after the relatively slow values related to the intercalation mechanism. As conclusion, they suggested a minor phenomenon of Na-ion adsorption

on pore surfaces at the end of the plateau region. This three stage model was also proposed in 2020 by Morikawa et al. [46] for HC produced from sucrose. Ex situ small and wide-angle X-ray scattering (SAXS and WAXS, respectively) revealed the formation of pseudo-metallic sodium in the nanopores and a relevant contribution of this phenomenon to the reversible capacity of the electrode. Recently, Zhang and coworkers [47,48] updated this mechanism when, after discharging the battery to ≈0.40 V, they found a peak in the Raman spectrum. This peak located at 1450 nm is characteristic of Na-C compounds, suggesting that sodium begins the intercalation before to achieve the plateau region. The authors proposed a reformulated mechanism: first, Na ions are adsorbed on the pores and defect sites; at 0.40 V Na ions begin to be intercalated into the HC and, when the voltage reaches 0.10 V, the filling of the nanopores starts to take place. It should be pointed out that during the low-voltage plateau, both Na intercalation and nanopore filling can occur simultaneously.

iv) Four stage model. In 2019, Alvin et al [49] attached a fourth step (adsorption on micropores prior to the intercalation step) to the three stage model. Lignin-derived HC was used and ex situ nuclear magnetic resonance (NMR) spectra and Na-ion diffusion coefficients revealed a partial micropore filling occurred in the sloping region between 0.2 and 0.1 V, after the adsorption of Na^+ on the high-energy surface defects and edge sites. In the plateau region below 0.1 V, Na ions were intercalated into the graphitic layers and a secondary adsorption of sodium in the micropores occurred near the cutoff potential. In addition, clustering and formation of metallic Na-Na bonds in the micropores were found when voltage decreased below 0.1 V.

v) Extended adsorption–insertion model. Sun et al. [50] proposed the "extended adsorption-insertion" mechanism after studying the microstructure of ginkgo leaves-derived HC produced over a wide range of pyrolysis temperatures (600–2500 °C). From lowest to highest temperature, three types of HCs microstructures gradually appeared:

(1) Highly disordered carbon with d_{002} larger than 0.40 nm. This interlayer distance is large enough for Na^+ to freely transfer via a "pseudo-adsorption" mechanism, contributing to the sloping region capacity together with the storage into conventional defects as pores, edges, and heteroatoms.
(2) Pseudo-graphitic carbon with d-spacing of 0.36–0.40 nm, which allows the interlayer insertion/desertion mechanism and contributes to the low-potential plateau, with a theoretical insertion capacity is 279 mA h g^{-1} corresponding to the formation of NaC_8.
(3) Graphite-like carbon with d_{002} below 0.36, which is too small to enable Na^+ insertion. Structural evolution of the carbon microcrystallinity was confirmed by XRD, HRTEM, and Raman spectroscopy; whereas kinetics analysis confirmed a diffusion-controlled process in the plateau region and a non-diffusion limited process in the sloping region. The best results regarding capacity, as well as rate and cyclic performance were obtained for hard carbons pyrolyzed at 1200–1300 °C, in which interlayers larger than 0.40 nm and between 0.36 and 0.40 nm coexisted, offering both "pseudo-adsorption" and "interlayer insertion" storage capacities.

vi) Adsorption-filling model. Zhang et al. [51] studied in 2016 the storage process in carbon nanofibers during sodiation and no shift of the (0 0 2) peak was observed when in situ XRD was performed. Hence, they discarded the sodium intercalation between graphene layers and proposed the adsorption-filling mechanism. The plateau region (below 0.1 V) was ascribed to the nanopore filling, since this region becomes the most prominent for carbons having greater amounts of small mesopores (around 3.2 nm). The slope region (1.0 to 0.1 V) was linked to the adsorption of sodium ions on the surface of graphene sheets. Li et al. [52] supported the "adsorption-filling" mechanism in light of the results obtained for cotton-derived HC. The TEM images of both pristine and sodiated HC revealed no differences in the microstructure, with similar interlayer spacing (0.404 nm) for both samples. Two years later, Bai et al. [53] corroborated this mechanism for sucrose-derived HC when they observed that (a) the low-voltage plateau disappeared after filling the micropores with sulfur, and (b) the sloping capacity was reduced when higher treatment temperatures (leading to lower amounts of defects and heteroatoms) were applied.

There is no doubt that discrepancies between models can partly be ascribed to differences in hard carbon structure, which strongly depends on both the biomass precursor and carbonization process conditions. Nonetheless, there seems to be a certain consensus about the existence of an adsorption-driven storage process associated to the slope region, showing this surface adsorption higher kinetics than the storage process at the plateau region. Is in this plateau where doubts appear regarding the processes taking place around the interlayer spaces and pores. The achievement of a detailed knowledge about all phenomena taking place during sodiation is crucial to reach a rational design of hard carbons and produce competitive anodes for SIBs. The objective must be maximizing the sodium storage capacity and be able to modify the electrode performance according to the battery requirements for a given use. Therefore, contributions from all the sodium storage sites must be considered and controlled by selecting the appropriate carbon precursors and tuning the structure, porosity, and surface chemistry of resulting HCs.

3. Plant-derived hard carbon anodes for SIBs

Selection of the biomass source is decisive since different plant precursors lead to different hard carbons, having unique structural and chemical properties and dissimilar sodium storage capacities. In order to achieve a proper anode performance, low-ash and high-carbon content HCs have to be selected. The natural microstructure of biomass is also a determining factor since it remains after carbonization and strongly affects to the electrochemical properties of the resulting carbon. Hence, different plant tissues may give rise to different nanostructured carbon materials with zero-dimensional (0D) spherical structures, one-dimensional (1D) nanotubes, two-dimensional (2D) nanosheets, or three-dimensional (3D) hierarchical structures. For instance, the carbonization of blue-green algae [54] led to a HC with an spherical morphology, while hollow tubular structures where obtained from cotton [55], bamboo [56], and kapok fibers [57]. Both structure types facilitate the electrolyte penetration and reduce the Na^+ diffusion distances. On the other hand, 2D sheet-shaped HCs —which were obtained from cherry petals [58], garlic peels [64], and cucumber stems [59]— also provide short paths for Na ion transportation and large surface areas for sodium ion adsorption [60].

However, hard carbons with 3D structures are the most commonly obtained when plant tissues are carbonized. The inherit channels and pores, originally used to transport moisture and nutrients, form an interconnected porous network that allows the electrolyte to enter the bulk and provides more sodium pathways and storage sites in the resulting HC. The pattern known as honeycomb-like structure usually appears when the cell walls remain, acting as a highway for the electrolyte (e.g., pine pollen [61], wheat straw [62], poplar wood [63], cork [64], and apricot shell [65]). In addition, these channels and cavities can buffer the volume expansion during charge/discharge cycles [66] and enhance the porosity-tailoring procedures described in Section 3.3 (e.g., reagents adsorption during wet impregnations for chemical activations). Note also that too high specific surfaces may be problematic when they result in low initial coulombic efficiency (ICE) values due to the enhanced solid electrolyte interface (SEI).

Plant-derived biomass include a wide variety of lignocellulosic tissues and its composition has also a considerable influence on the final HC electrochemical properties [67]. The three basic components of plants are cellulose and hemicellulose (long and short-chain polysaccharides), together with lignin, a complex phenolic polymer. Cellulose microfibrils are the main structural element, which are aligned and attached with hemicellulose, lignin or also pectin to form fibril aggregates or macrofibers [68].

During the carbonization process, these lignocellulosic compounds are decomposed by dehydration, decarbonylation, and decarboxylation to form the carbonaceous material [69]. Cellulose and hemicellulose decompositions are known to take place in the ranges of 300–400 °C and 200–300 °C, respectively, while the more stable lignin is decomposed in a wider range of temperatures from 250 to 900 °C [70]. The release of small molecules (CO_x, CH_4, H_2O, H_2) and volatiles during those reactions determines the char porosity. Decomposition of abundant adjacent hydroxyls in both cellulose and hemicellulose produces micropores, while the aromatic *p*-hydroxyphenyl, guaiacyl, and syringyl units from lignin promote robust and non-microporous structures [71]. This explains why herbaceous-derived carbons usually exhibit higher surface areas than the more lignified wood-derived materials [72]. On the other hand, hemicellulose and lignin are highly crosslinked and noncrystalline, thus producing nongraphitic carbons when pyrolyzed [73]. Conversely, the anisotropic nature and abundant intra and intermolecular hydrogen bonds of cellulose result in a more packed structure, higher crystallinity and better thermal stability [74]. Hence, a proper cellulose and hemicellulose-lignin ratio is desirable to ensure enough ordered graphitic layers but, at the same time, avoiding an excessive graphitization [75].

Inorganic elements in biomass such as potassium, calcium, and silicon, also have a considerable impact on the electrochemical properties of the resulting HC. Saavedra et al. [76] analyzed the influence of the polymeric and inorganic composition of different feedstocks on the final carbon. They pyrolyzed a resinous wood (pine), a deciduous wood (beech), an herbaceous plant (miscanthus) and a cereal waste (wheat straw) at 1400 °C. The pine wood-derived carbon had the highest lignin content (27.5%) and showed the best electrochemical performance, with a first reversible capacity and ICE of 300 mA h g^{-1} and 85%, respectively. On the other side, miscanthus and wheat straw-derived carbons exhibited the worst performances in terms of reversible capacities (240 and 200 mA h g^{-1}) and ICE (70% and 60%). Saavedra et al. ascribed the low reversibility of these biomass sources to the higher content in inorganic species, since they can occupy active sites as well as contribute to unwanted reactions [72]. As further discussed in Section 3.1.3, washing procedures are recommended to prevent and mitigate this problem.

3.1. Hard carbon production

The conversion of plant-derived biomass into hard carbon is based on thermochemical processes, such as pyrolysis and hydrothermal carbonization (HTC). Operating variables, together with the choice of plant precursors, have a strong influence on the final HC properties.

3.1.1. Pyrolysis

To date, pyrolysis is the most common procedure to produce biomass-derived carbons. In this process, biomass is heated under an inert atmosphere to be decomposed into three fractions: char, volatiles, and permanent gases. Slow pyrolysis —with heating rates and peak temperatures typically ranging from 1 to 30 °C min^{-1} and from 350 to 700 °C, respectively— is a well-known technique to produce charcoal or biochar. The term biochar applies when it is used as carbon-rich soil amendment for long-term carbon sequestration purposes [77]. Biochar can also be activated and/or functionalized to be used in a number of potential value-added applications, including electrochemical energy storage [78,79].

As will be discussed in Section 3.2, treatment temperatures higher than 1000 °C are usually required to obtain HCs with an enough ordered structure to be used in electrochemical applications —see Table S1 in the Supplementary Information (SI)—. To this aim, two production strategies can be adopted: one- and two-step carbonization processes. The former consists of a single pyrolysis step at the desired final temperature, while in the two-step carbonization approach, a previously made biochar is heated again through a second pyrolysis step [80,81]. Alvin et al. [82] assessed the effects of using these two production pathways (until 1000–1500 °C) for fir wood as feedstock. They underlined that, in the one-step direct pyrolysis, carbon atoms might not have time enough to reorganize, leading to a pseudographitic structure; for its part, the two-step carbonization process can provide more pseudoequilibrium hexagonal carbon planes embedded in the amorphous carbon region. As a result, two-step strategy provided best ICE, reversible capacity, and high-rate performance.

Besides peak temperature, inert gas nature can also influence the final carbon properties. Nitrogen (N_2) is the preferred inert gas when low-temperature pyrolysis is carried out, for example to produce biochar. Argon (Ar), however, is usually selected to produce HCs at higher temperatures (e.g., for electrochemical purposes), since N_2 can slightly be oxidized at temperatures above 1000 °C. Marino et al. [83] studied the influence of the Ar or N_2 annealing atmospheres and they did not found significant differences on the physicochemical and electrochemical properties of almond shells-derived carbons produced at 1000 °C. The same was reported by Xu et al. [84] for hornet nest-derived carbons produced at 1000 °C. However, at higher temperatures (1200–1400 °C), carbons prepared under argon atmosphere offered lower specific surface area and higher ICE, capacity retention, and rate capability.

Additional operating parameters, such as gas flow rate and heating rate, can also affect the specific surface area of carbons. For instance, using relatively high flow rates reduce the residence time of released gas (rich in CO_2), decreasing the extent of the reverse Boudouard reaction and the related carbon porosity development [85]. On the other hand, using relatively slow heating rates allows the produced gas to fully escape from the particle, resulting in a certain closure of micropores and, consequently, in an improved ICE and capacity retention [86].

3.1.2. Hydrothermal carbonization

Hydrothermal carbonization (HTC) is a thermochemical process in which biomass is heated in a water suspension at relatively low temperatures (less than250 °C) and under saturated pressure. HTC process is inspired by the natural coal formation and its five reaction mechanisms are hydrolysis, dehydration, decarboxylation, aromatization, and condensation polymerization [87]. HTC is an attractive procedure because of its low cost and mild synthesis conditions [88].

Despite the fact that hydrochar (i.e., the carbon material produced by HTC) does not meet the required properties to be used as electrode material, a cascaded HTC-pyrolysis process could be highly interesting to produced engineered carbons. For instance, Zheng et al. [89] used HTC at 180 °C followed by pyrolysis at 800 °C to produce holly leaf-derived HC. HTC process enlarged the pores of tiny graphite-like domains compared with the direct pyrolysis strategy. Since large nanopores proved to be beneficial for Na-ion transfer and storage, HTC derived carbon provided better reversible capacity (318 mA h g^{-1} at 0.02 A g^{-1}) than the direct pyrolysis HC (112 mA h g^{-1}). Wang et al. [90] also reported positive results (372 mA h g^{-1} at 0.025 A g^{-1}) when reed straw was hydrothermally carbonized at 200 °C and then pyrolyzed at 1300 °C (see Table S2). In addition, hydrothermal reaction of macromolecule monomers is known to form surface nanospheres [91,92], whose aggregation origins holes and channels and facilitates electrolyte penetration and Na^+ intercalation. HTC is also appropriate to remove biomass impurities, avoiding the need of acid or alkali washing procedures. Finally, as shown in section 6.3.1, chemicals can be added to the aqueous solution to modify carbon structures by promoting certain decomposition reactions.

3.1.3. Removal of inorganic species

As previously discussed, inorganic elements can remain in HCs and worse its sodium storage capacity. Zhang et al. [80] evaluated the effect of impurities on the electrochemical performance of pinecone-derived HC anodes, which were produced by a two-step carbonization method. After the first pyrolysis step at 500 °C, the resulting char was dispersed

into 20 wt% KOH aqueous solution at 60 °C, filtered, dispersed under stirring in a 3 M HCl solution at 60 °C for 5 h, and finally rinsed by deionized water. Once dried and carbonized at 1400 °C, the inorganic elements content in the final hard carbon (Mg, P, S, K, Ca, and Si) decreased under the SEM-EDX detection limit. The ash content was also reduced from 1.46 wt% in the unwashed HC to 0.008 wt%. Zhang and coworkers also observed that the plateau capacity significantly decreased along cycles for the unwashed HC anode, because impurities occupied some sodium storage active sites. The measured capacity after 100 cycles was 328 mA h g^{-1} and 299 mA h g^{-1} for the washed and unwashed HC, respectively.

Hydrochloric acid (HCl) is the most used washing agent to produce hard carbon for SIBs. Dahbi et al. [41] studied the HCl-washing of raw argan shells to remove inorganic species before pyrolysis. After been washed with acetone, argan shells were treated with 2 M HCl for 20 h at 60 °C, and finally washed with deionized water. X-ray fluorescence (XRF) spectra indicated that HCl treatment could not eliminate heavy metals such as Ni, Co, Fe and Zn, but eliminated K completely. Moreover, HCl treatment contributed to an increase in the BET surface area of the resulting HCs, which also exhibited a larger number of active sites due to the promotion of defects and/or voids. As a result, the argan shell-derived HC —which was produced via washing with HCl and subsequent pyrolysis at 1200 °C— delivered a reversible capacity of 333 mA h g^{-1}, a 12.5% higher than that obtained for the HC produced from the unwashed precursor. Alternative agents such as hot water, HF, H_2SO_4, NH_4HF_2 and ethanol have also been used by other authors to wash biomass and/or the produced carbon (see Table S6).

3.2. Highest carbonization temperature

Hard carbon graphitization degree, heteroatom presence, and porosity are strongly influenced by the highest carbonization temperature. Zhang et al. [51], who assessed the temperature effect on polyacrylonitrile-derived HC nanofibers produced at temperatures ranging from 650 to 2800 ℃, observed that HCs produced at relatively low temperatures showed a microporous structure and a poor stacked C–C aromatic structure. By contrast, carbonization at higher temperatures improved the structure ordering by graphene layers growth, while ultramicropores and heteroatoms were gradually removed. Moreover, mesopores (Ø > 2 nm) were developed via the release of CO_x and HCN gases from the decomposition of functional groups, but also due to the rotation of the graphene layers. As a general rule, microporosity in lignocellulosic-derived carbons shows a maximum value at around 800 °C, from which the surface area starts to decrease due to the structural order increase [93].

Zhang et al. [44], who produced lotus stem-derived HCs at highest temperatures varying from 1200 to 1600 °C, reported that an increased carbonization temperature resulted in the removal of heteroatoms and the improvement of the local structure ordering. By means of N_2 adsorption/desorption isotherms, they also determined how the increasing temperature concentrated the pore size distributions in the range of 2–4 nm and reduced the specific surface area and the number of open pores. Similar effects of the carbonization temperature on porosity was noticed by Sun et al. for ginkgo leaves-derived HC [50]. Ultramicropore area from CO_2 adsorption isotherms showed a volcano-shaped tendency with a maximum value at 800 °C, while BET surface area (from N_2 isotherm) had a maximum value of 242 m^2 g^{-1} at 1200 °C, ascribed to the complete release of small molecules. Then, BET area diminished until 16 m^2 g^{-1} at 2500 °C together with the growth of the graphitic crystallite. Structural ordering with temperature is possible since carbon atoms have enough energy to realign themselves. Furthermore, the stronger van der Waals interaction between adjacent graphene layers can also promote ordering [82]. Textural densification at high temperatures results in the pore structure collapse and the above-mentioned low surface areas [94]. It should also be noted that higher graphitization is also linked to an increase in the electronic conductivity, due to the reduction of oxygen heteroatoms and the improved crystallinity of the HC [75,95].

Recently, Yu et al. [96] reviewed more than 20 articles focused on plant-derived HCs and conclude that temperature determines the pore size distribution, specific surface area and degree of graphitization. As previously discussed, higher temperatures promote graphitization and thus decrease the hard carbon interlayer spacing. In addition, the specific surface of the HC decreases with temperature, leading to less electrolyte decomposition and higher ICE. Since the maximum reversible intercalation of Na^+ is reached for an interlayer space around 0.40 nm, there is an optimal temperature value for each biomass feedstock, generally between 1000 and 1400 °C, at which the storage capacity can reach its maximum value. Fig. 5 plots the reversible capacities reported in 57 previous studies on plant-derived HCs (see Tables S1 and S6 for full details). Reversible capacities in the range of 200–400 mA g h^{-1} and ICE values above 60%–90% were reported. At this point, it should be pointed out that biomass feedstock can strongly affect the anode capacity, in the light of the relatively wide range of capacities reported for electrodes prepared following similar carbonization procedures and preparations.

Regarding the porosity, researchers usually link high BET surface areas with severe SEI formation and subsequent low ICE values. Nevertheless, this connection is not as simple as it may seem since BET surface area does not mean electrochemical active surface area. As an example, Zheng et al. [63] produced poplar wood-derived HC at different temperatures and reported that two HCs having BET surface areas of 5.8 and 117 m^2 g^{-1} showed almost equal ICE values of 88.3% and 87.0%, respectively. The authors observed that, for the HC exhibiting the highest surface area, the porosity was mainly due to narrow micropores of around 1 nm, which were probably not covered by the SEI. Zheng and coworkers concluded that, even if narrow micropores were electrically conductive and accessible by electrolyte, the resulting SEI was hardly formed in them as well as very thin. Therefore, ascribing low ICE values exclusively to high BET surface areas may be inappropriate. Other factors such as the pore size distribution and the availability of functional groups on the surface of HC should also be considered. In line with this, Yang et al. [97] observed that the electrolyte was unable to penetrate inside a ultra-microporous (0.3–0.5 nm) HC electrode, leading to more available active sites for Na^+ storage and enabling a relatively high ICE value of 80%.

Another relatively new approach to understand the electrochemical performance of HC anodes relates to the percentage of open and closed pores [98,99]. “Open pores” are those connected with the external surface, while “closed pores” are isolated voids inside the material. Closed pores can store Na^+ ions and simultaneously avoid the SEI

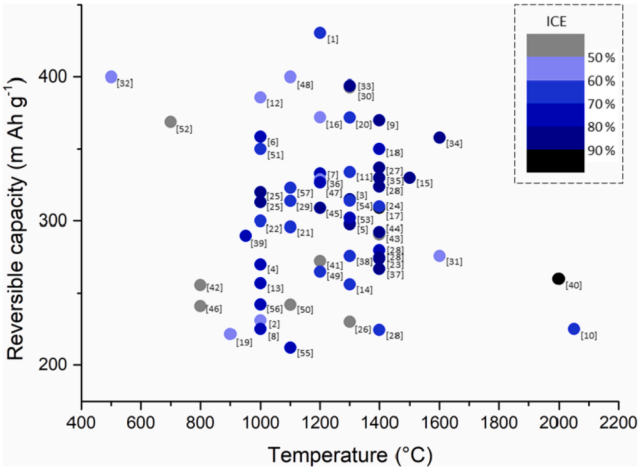

Fig. 5. Reversible capacities obtained for different plant-derived hard carbon anodes in SIB half-cells. Data and references are included in Table S1.

growth, since they are not in contact with the electrolyte. Na metal clusters seem to be preferably deposited into the closed pores, contributing to the sodium storage plateau capacity [44]. As the carbon is reduced and the Na^+-C interaction turns less ionic, the charge transfer to the Na ions makes them more metallic and sodium pooling takes place. This phenomenon is favored in closed pores, because sodium ions around are in a solid state without solvent molecules [99]. The availability of closed pores is promoted when the highest carbonization temperature increases, due to structure arrangement that causes the folding of curved carbon layers and the coalescence of nanopores [64]. Moreover, some open pores can turn into closed ones when highly active carbon free radicals restore and rebuilt the conjugated carbon structure at high enough temperatures [100].

3.3. Tailoring porosity of hard carbons

Several strategies have been proposed to improve the sodium storage capacity of plant-derived HCs and/or reduce the highest carbonization temperature for their production (see Fig. 7). Activation processes could be useful to adjust the pore size distribution and simultaneously increase the specific surface area and the number of defects. It is generally agreed that a hierarchical pore structure —composed of micro-, meso- and macropores— provides easily accessible active sites for Na ions [101], shortening the ion diffusion distance and improving charge transfer kinetics [102,103].

Nonetheless, and as stated in the previous sections, large surface areas can lead to SEI growth and low ICEs, although pore size distribution can also condition the amount of SEI [63]. In addition, HCs having a hierarchical and interconnected porous structure can suffer from a fast electrolyte penetration, which can enhance the formation of a stable SEI film during the first cycle [104]. It should also be kept in mind that the low ICE values measured for some HCs is also related to the irreversible sodium trapping in functional groups, defects and between the interlaying spacing [65,94,105]; therefore, they cannot be only attributed to the porosity and SEI [106].

In order to build tuned and hierarchical porous structures, with honeycomb or sponge-like morphologies, physical or chemical activation processes can be applied. For physical activation, steam and CO_2 are typical activation agents, whereas KOH, H_3PO_4 and $ZnCl_2$ are the most used compounds for chemical activation purposes [107].

3.3.1. Chemical activation

Chemically activated HCs can be produced via two different procedures. On the one hand, the activation agent can be mixed with the raw biomass to conduct a simultaneous pyrolysis-activation or HTC-activation process. This can be done through a dry mix or by impregnating the biomass with an aqueous solution of the chemical agent. On the other hand, the chemical agent can be blended with a previously made carbon (e.g., biochar or hydrochar) and subsequently carbonized. As can be seen in Table S3, both biomass and char activations have been used to produce plant-derived HCs. The most common chemical agents and their effects on the textural features of resulting chemically activated carbons are discussed below.

(i) Potassium hydroxide (KOH) is the most used agent to produce porous HCs. Recently, Chen et al. [108] have proposed a mechanism to explain the role of KOH during biomass pyrolysis. They suggested that KOH reacts with active O-containing species in biomass to remove most of the O-containing groups and form a number of vacancies. Moreover, KOH also reacts with more stable carbon fragments to generate vacancies. Then, OH– from KOH can quickly occupy these vacancies to introduce oxygen, forming large amounts of new O-containing groups in the biochar. KOH can also be transformed into K_2CO_3 at 400–600 °C, and then further converted to K_2O at 700–800 °C. At this temperature, the CO_2 released from the decomposition of K_2CO_3 can enhance the porosity growth via reverse Boudouard reaction. Moreover, metallic potassium, K_2CO_3 and K_2O can also react with carbon, leading to more voids and structural changes [109,110].

With regard to the carbon morphology changes, three mechanisms may occur [111]: (a) chemical etching to form pores, (b) carbon gasification with CO_2, and (c) lattice expansion due to the insertion of K^+ into the lattice planes. As a result, KOH-activated carbons showed interconnected carbon walls and interconnected macro-, meso- and microporous structures, which facilitate the access of electrolyte and reduce the high-rate diffusional losses. It has also to be mentioned that KOH activation tends to attack the graphitic domains, leading to more disordered carbon structures [112]. Furthermore, KOH activation seems to increase the content of carbonyl-containing functional groups in surface, providing more reversible Na^+ storage sites and higher specific capacities [113,114].

(ii) Phosphoric acid (H_3PO_4) is another common chemical agent used for activation purposes. In this case, H_3PO_4 incorporates phosphorous- and oxygen-containing functional groups on the carbon surface. The pseudocapacitive effect from theses functional groups can contribute to the energy storage [115,116]. Similar to KOH, H_3PO_4 activation partially consumes the graphite structure, develops a 3D-connected porous structure, and expands the carbon layer spacing. Dou et al. [117] also found that a prolonged acid pretreatment of the biomass (for 2 weeks), prior to its carbonization at a relatively low temperature of 800 °C, enhanced the structural order, micropore closuring, and mesopore growth of final HCs, thus avoiding the need of higher carbonization temperatures.

(iii) Zinc chloride ($ZnCl_2$) acts as a dehydration agent during biomass carbonization, resulting in HCs having higher aromatization degrees and crosslinked porous development. Contrary to the previous cases, carbon is not removed by the activation agent. Thus, carbon content is generally improved, despite higher surface areas than those obtained with KOH can be attached [118]. $ZnCl_2$ penetrates inside the material structure and works as a skeleton upon which a coral-like mesoporous carbon can be created. Additionally, microporous can appear on the carbon surface when gases scape from bulk reactions [119].

(iv) Other acids such as sulfuric and hydrochloric can also be employed as activation agents, since they catalyze the hydrolysis of lignocellulose biomass, leading to chars having an altered morphology, microstructure, and surface composition. Wang et al. [104] reported that chemical activation of platanus bark with H_2SO_4 was a successful method to obtain a hierarchically porous loose sponge-like carbon structure. Concentrated H_2SO_4 dissolved the cellulose and extracted impurities to form micropores, while the large carbon layers were fragmented into small sheets, giving rise to a mesoporous structure. In addition, an increase in the order degree and the interlayer spacing was observed. Similar results were found by Wang et al. [120] for HCl-treated lotus leaves.

As shown in Fig. 6, chemical activation allows to obtain suitable HCs

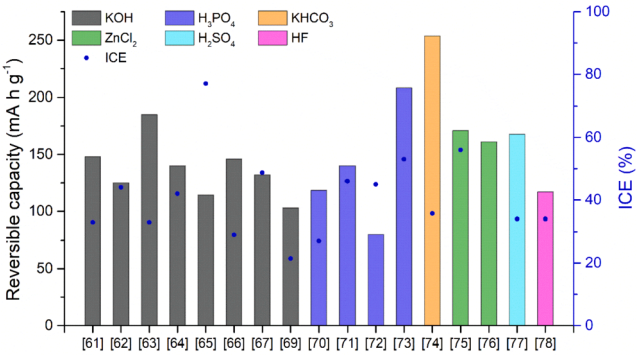

Fig. 6. Reversible capacities obtained for different activated plant-derived hard carbon anodes in SIB half-cells at a current rate of 1 A g^{-1}. Data and references are included in Table S3.

for SIBs at relatively low carbonization temperatures (600–800 °C). Decreasing the highest temperature is an industrial strategic advantage because it means a reduction in the energy consumption. Also outstanding is the improved high-rate capability of HC anodes, attributed to connected porous structures, stable pathways for ion diffusion, and more availability of electrochemically active functional groups on surface. Fig. 6 also shows how different plant-derived HCs, activated with diverse chemicals, deliver more than 100 mA h g^{-1} when are cycled at 1 A g^{-1} (full results are available in Table S3). On the contrary, the main disadvantage of chemical activation is the low ICE measured, even less than 40%. This problem could be attenuated by modifying the surface and pore size distribution of the HC, as well as by improving the binder formulation in the electrode and/or the electrolyte. Furthermore, the relatively low highest temperatures used can lead to carbons with low electronic conductivity and, therefore, poor capacity retention.

In addition to the above-explained common activation procedures, catalyzed HTC can also be conducted in a pure or dilute chemical agent solution to produce hydrochars with engineered properties (see Table S4). For example, apple pomace [121] and pistachio shells [122] were hydrothermally carbonized in 0.8 M KOH and 3 M NaOH, respectively, to further develop the porosity of the final HC. Furthermore, HCl and H_2SO_4 can also be used for catalytic HTC step, since acids can catalyze the hydrothermal hydrolysis, dehydration, condensation, and decomposition reactions of biomass [120], also contributing to insert surface oxygen-containing functional groups [102]. With this respect, it must be highlighted that C–O and C = O bonds can increase the adsorption capacity of sodium, although C–O bonds can also promote the irreversible sodium storage and subsequent low ICE [123,124]. Other chemical additives have been proposed for hydrothermal treatment; for instance, hexadecyl trimethyl ammonium bromide (CTAB) plus KOH (to reduce micropores and increase mesopores [125]), or H_2SO_4 plus H_2O_2 (to enlarge the interlayer spacing of graphitic domains [62]).

3.3.2. Physical activation

The addition of CO_2 into the feed gas stream during thermal treatment induces the porosity development through the reverse Boudouard reaction. Kumaresan et al. [126] carbonized *Borassus flabellife* inflorescences in a CO_2-N_2 gas mixture (up to 10 vol% CO_2) at 1400 °C. The physical activation promoted rough surface, wrinkles, and broken edges, together with a pore growth between turbostratic nanocrystallites. Regarding the electrochemical performance, the notable rise in the plateau capacity (about 70%–75%) was ascribed to the improved interlayer spacing, while no significant variation in coulombic efficiency was observed. When the feed gas was composed of 5 vol% CO_2, reversible capacities of 358 and 151 mA h g^{-1} were measured at 0.02 and 1 A g^{-1}, respectively (the nonactivated HC performed 272 and 81 mA h g^{-1}, respectively). Despite this, physical activation is less common than chemical activation in this field and, to our knowledge; no more CO_2-activated HCs have been tested for SIBs.

Physical activation with air is also an alternative to develop the porous structure. Ding et al. [43] activated a previously made peat moss-derived HC under air flow at 300 °C for 3 h, increasing the BET surface area from 24.5 to 196.6 m^2 g^{-1}. Despite the difference in porosity, not appreciably effects on the graphitic order/disorder or surface composition were observed. Moreover, similar reversible capacities were obtained when the half-cell was cycled under a current density of.

0.05 A g^{-1}: 325 mA h g^{-1} (60.7 % ICE) for the nonactivated HC and 332 mA h g^{-1} (57.5 % ICE) for the activated HC. Nevertheless, as also observed for chemical activation, a notably greater improvement was achieved for the rate capability. When the current density increased to.

0.5 A g^{-1}, the activated HC delivered a reversible capacity of 203 mA h g^{-1}, 89% higher than that measured for the nonactivated one. Moreover, cycling capacity retention was also improved because pores could buffer the sodiation-induced expansion/contraction and the subsequent damage of the electrode. HCs from banana peels [73] and lotus petioles [127] were also produced via carbonization at 1100 ℃, with a preliminary step consisting of air activation at 300 ℃. The resulting carbons delivered around 150 mA h g^{-1} when were cycled at 1 A g^{-1} (see Table S3).

To sum up, a broad diversity of chemical and physical activation techniques is available to tune hard carbon structures in accordance with the desired electrode destination. One or even various techniques can be selected in each case, particularly with the aim at improving the high-rate capability. For example, activation with air of a previously chemically activated carbon was proposed to develop additional porosity [128]. An acid-catalyzed HTC step followed by KOH activation can be employed to obtain a more ordered pseudographitic structure with higher surface area and more surface oxygen-containing groups [112,113].

3.3.3. Other strategies

Besides chemical and physical activations, other strategies have been proposed to tailor the microstructure of HCs in order to improve their electrochemical performances.

(i) Microwave activation. Exposure to microwave radiation generates thermal and molecular vibration effects on plant-derived HCs, improving the graphitization degree and creating slit pores among microcrystals. Yu et al. [129] activated a sugarcane-derived HC in a 0.2 M HCl solution via microwave heating at 1500 W for 1 h. As a result, enhanced porosity —according to both CO_2 and N_2 isotherms— and an improved reversible capacity of 323.6 mA h g^{-1} at 0.05 A g^{-1} were achieved [129].

(ii) H_2 reduction. This method was proposed to reduce the defects of HCs and then improve the microcrystalline structure [65]. An apricot shell-derived HC produced at 1300 ℃ was then treated for 2 h under a H_2/Ar hybrid atmosphere (7:93 v:v) at 800 ℃. This process improved the reversible capacity from 363 mA h g^{-1} to 400 mA h g^{-1} and the ICE from 69% to 79%, when the half-cell was cycled at 0.025 A g^{-1} [65].

(iii) High current pretreatment. A high current charging-discharging process was applied to a hemp haulm-derived HC (which was produced via carbonization at 600 ℃) to reconstruct its surface structure. After a number of charge-disharge cycles at 1.8 A g^{-1} in a half cell, the low-energy Na ions bombardment resulted in a more ordered surface structure and to a certain rearrangement of the superficial graphitic layers. As a result, an improvement in the plateau capacity and the high-rate capability was reported. This procedure increased the anode capacity from 101 mA h g^{-1} to 256 mA h g^{-1} when was measured at a current density of 0.374 A g^{-1} [130].

(iv) Presodiation to improve ICE. Irreversible trapping of Na ions together with an excessive growth of the SEI layers usually lead to low ICE values. Presodiation of HC anodes in half cells before the full cell assembly is a common technique to mitigate the effect of low ICE. However, this process, in which the anode must be extracted and then moved to the full cell, is not practical at industrial scale [131]. As an alternative, Xiao et al [132] proved the effectiveness of commercial stabilized lithium metal powder (SLMP) for a SIB prototype, reaching an ICE improvement from 70.3% to 92.1% when SLMP was added to a commercial HC. Recently, also chemically presodiation techniques are being studied for HC anodes. Sun and coworkers [133] sprayed a sodium naphthaline solution onto a hard carbon electrode achieving an ICE improvement from 67% to 87%. Conversely, Liu et al. [134] immersed a HC electrode in a sodium biphenyl solution for 1 min reaching an ICE improvement from 70% to 100%.

(v) Exfoliation to create 2D materials. Two-dimensional materials (e.g., graphene and transition metal sulfides/selenides) are gaining popularity due to their unique 2D-layered structure with infinite planar lengths, that provides short paths for Na diffusion and large surface area for sodium ion adsorption [60]. To our knowledge, 2D plant-derived HCs have not been studied as anodes for SIBs yet. However, some exfoliated plant-derived HCs with high capacitances and energy densities were studied for the field of supercapacitors. Recently, carbon

nanosheets were obtained through a room temperature H_3PO_4 exfoliation from a previously KOH-activated nettle stem-derived HC [135]. Exfoliated corn cob-derived HC was also produced by its oxidation in concentrated HNO_3 for 4 h and the subsequent thermal exfoliation via a flash heat treatment (45 s) at 950 ℃ [136].

3.4. Hard carbon doping

In addition to the activation processes described above and the use of conductive additives, HC doping could also improve the intrinsic HC electronic/ionic conductivity. Furthermore, doping can promote structural changes that can boost the electrochemical sodium storage properties [137]. Dopants can increase the interlayer spacing, act as active sites, and produce charge distortions on the HC surface atoms [138,139], being an effective method to accelerate transfer and reaction kinetics to produce SIB electrodes with higher power density and storage capacity.

3.4.1. Heteroatom doping

Nonmetal element doping is widely used when HCs are produced from synthetic organics, since dopants can easily be added by using special precursors. Concerning plant-derived HCs, nonmetal doping is at an early stage and is usually conducted on a previously chemically activated HC. A dopant source compound is mixed with that carbon and then the nonmetal heteroatoms are attached to the carbon structure via an annealing process (see Table S5). It should be pointed out that, in many articles, "doped hard carbon" refers to the heteroatoms already available in the raw biomass. In our opinion, it should not be considered a doped HC since all biomasses contain —to a greater or lesser extent— nonmetal elements (N, S, P, etc.) and it can be confused with the process described herein.

Coming back to the carbon enhancement, two types of dopants can be added to modify the carbon charge distribution. Donor or n-type dopants act as electron donors, while acceptor or p-type dopants has a deficit of electrons and originate positive holes [16]. The most used nonmetal dopants are nitrogen, sulfur, phosphorus, boron, and fluorine.

(i) Nitrogen is the most extensively investigated heteroatom dopant. It shows three common bonding configurations within the carbon lattice, including pyridinic-N, pyrrolic-N, and quaternary-N (or graphitic-N) [140]. Pyridinic-N and pyrrolic-N introduce carbon vacancy defects that originate electron acceptor states to gain electrons from Na atoms (see. Fig. 8). Quaternary-N introduction, however, does not promote sodium storage because does not create edges or vacancy defects able to accept more electrons [141]. Urea [139] and ammonia [142] doping were investigated as compounds to add nitrogen functional groups in synthetic HCs. Regarding plant-derived carbons, hemp fibers [143] and onion wastes [144] were doped via HTC with urea solutions. In the former case, HTC doping was conducted on a HC previously activated with KOH, reaching an ICE improvement from 34.8% to 44.9%. In the second article, the onion waste was directly hydrothermally treated in a urea solution and then annealed at 800 ℃. When cycled at 1 A g^{-1}, nondoped and doped HCs showed reversible capacities of 26.9 mA h g^{-1} and 120 mA h g^{-1}, respectively. In other study, a grapefruit peel-derived HC was produced via carbonization at 600 ℃, then impregnated with

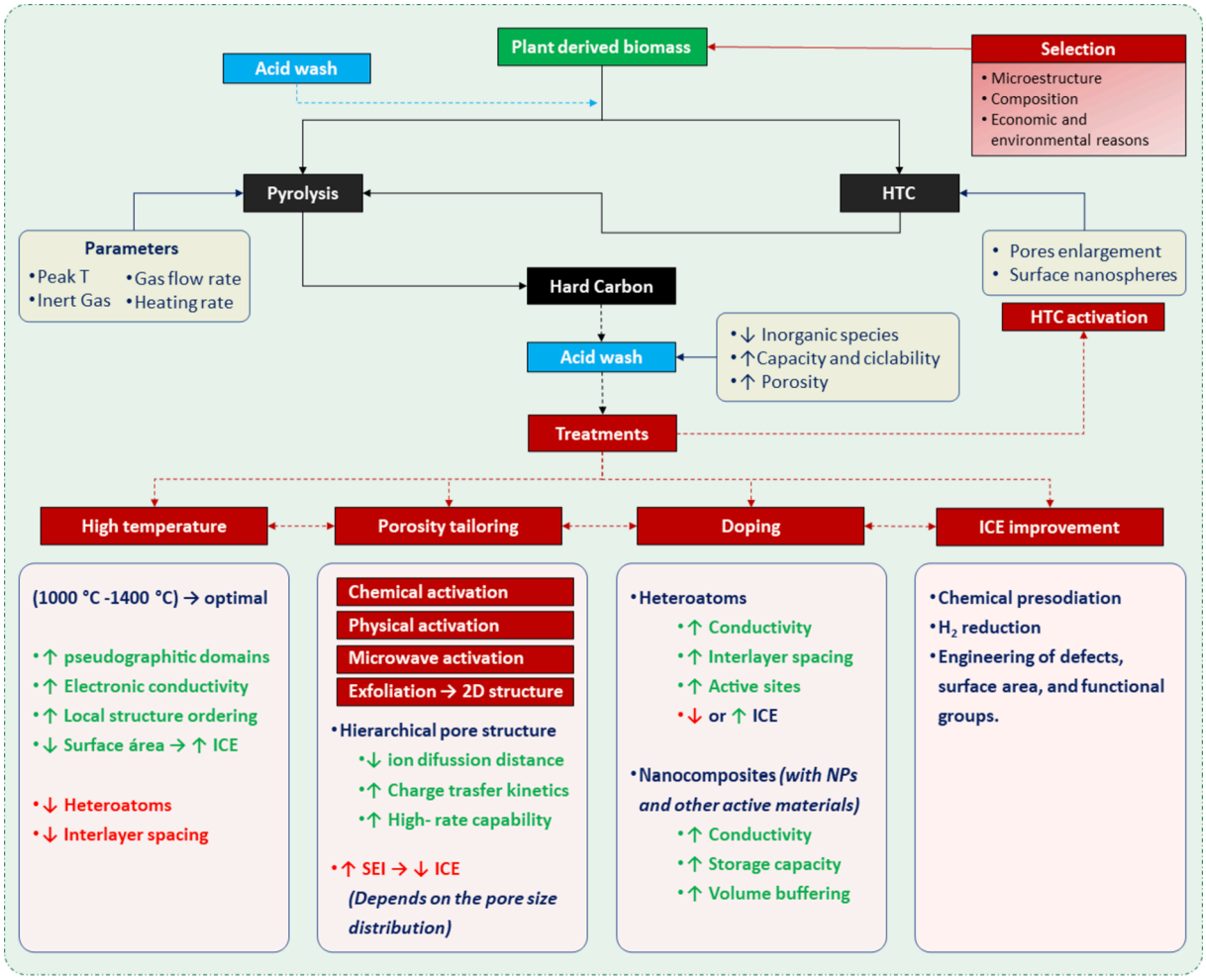

Fig. 7. Schematic diagram summarizing the treatments that can be used for producing engineered plant-derived hard carbons for SIBs.

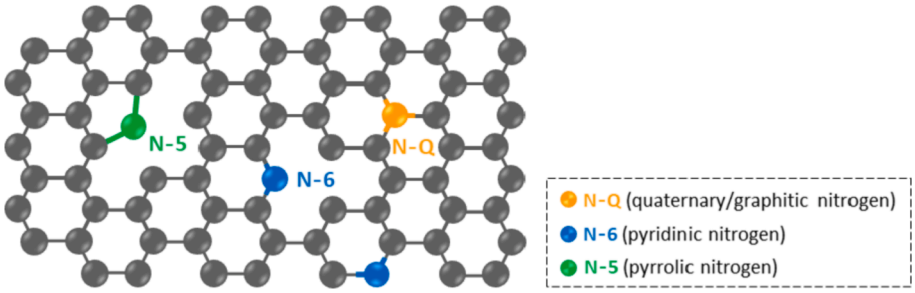

Fig. 8. Pyridinic, pyrrolic and quaternary nitrogen in a doped carbon lattice. Source: authors' own creation.

urea, and finally annealed at 600 C [145]. Despite the low annealing temperature, a reversible capacity of 172 mA h g^{-1} was reported for a current density of 0.037 A g^{-1}. Ethylenediamine was also used to dope a mango-derived HC via impregnation with methanol at room temperature [146]. This HC, previously produced by acid-catalyzed HTC and several oxidation steps, delivered impressive reversible capacities of 445 mA h g^{-1} and 162 mA h g^{-1} at current densities of 0.02 A g^{-1} and 1 A g^{-1}, respectively. More information is available in Table S5.

(ii) Sulfur doping increases the interlayer distance of carbon due to its larger covalent diameter, improving the Na^+ intercalation capacity. Moreover, sulfur creates C–S_x–C (x = 1, 2) electrochemically active covalent bonds, improving electronegativity of HC and also the reversible storage of sodium ions. The bond cleavage and the rearrangement of sulfur atoms during the discharge/charge cycles allow the Na^+ ions to be accommodated and improves the cell reversible capacity [147,148]. Because safety risks, gaseous sulfur sources are usually avoided and solid or liquid-state sulfur sources are mixed with the undoped materials before the annealing process. Elemental sulfur [147] and 2-tiophenemethanol [149] were used with bacterial cellulose and durian shell, remarkably increasing the sodium storage. The durian shell-derived HC treated with 2-tiophenemethanol delivered a reversible specific capacity of 264 mA h g^{-1} after 200 cycles at 0.1 mA g^{-1}, a 52.6 % increase over the equivalent nondoped carbon.

(iii) Phosphorus is an n-type dopant that induces localized electronic states and improves the electronic conductivity of HC. Due to its bigger atomic radius, also enlarge the interlayer distance. Furthermore, since P–C bond is 24.6% longer than the C–C bond, P atoms cannot be housed in the two-dimensional graphitic lattices and give rise to pyramidal-like structures [150,151]. P-doped HCs were produced from Artemia cyst shells [152] and horse chestnut leaves [153] by H_3PO_4 impregnation prior carbonization. The latter biomass was impregnated with a H_3PO_4 solution (mass ratio of H_3PO_4 to leaves of 3) and then carbonized at 500 ℃. The resulting HC delivered a reversible capacity of 326 mA h g^{-1} at 0.1 mA g^{-1}, substantially higher than that delivered by the nondoped HC (112 mA h g^{-1}).

(iv) Boron is a p-type dopant that improves the electrostatic adsorption of sodium while produces a slight lattice expansion (B–C bond = 1.50 Å). The adsorption energy of Na on B-doped graphene was found to be –1.93 eV, about 2.7 times than that of essential graphene (–0.71 eV). This results in more stable Na^+ adsorption sites, where each B atom in the graphene can adsorb until three sodium atoms [154]. This high-binding energy should be treated with caution since could lead to irreversible adsorption in the first charge/discharge cycle [137]. Boric acid [155] and boron tribromide [156] were used to dope graphene oxide and graphitic carbon. However, no articles focused on B-doped HCs were found.

(v) Fluorine has the strongest electronegativity of the previously described elements (χ = 3.98 of F vs. 3.04 of N). Thus, in addition to the possibility of enlarging the interlayer spacing of HCs, F-doping can reduce the energy barrier for Na^+ insertion [157]. F_2 gas [158] and hydrofluoric acid [159] have been used to dope carbon in the supercapacitors field. However, to our knowledge, fluorine doping has not been tested yet for HC-based electrodes in SIBs.

Furthermore, dual heteroatom doping is an interesting option to gain synergies between the doping elements. For example, N-S dual doping merges the carbon surface defects induced by N with the interlayer spacing and active sites created by S. Thiourea [160,161], rhodamine [162], trithiocyanuric acid [163], ammonium sulphate [164], and thioacetamide [165] have been used to dope synthetic HCs. Moreover, thiourea doping of a tangerine peel-derived HC [166] and a cotton-derived HC [167] were reported. The latter study —where cotton was immersed in a thiourea solution, carbonized at 800 ℃, and activated in air at 300 ℃— reported a successful reversible capacity of 351 mA h g^{-1} for the 600th cycle at 2 A g^{-1}. N-P dual doping can also be suggested to create a more defective structure and larger interlayer spacing. $(NH_4)_2HPO_4$ was employed as doping agent to dope a corn stalk rind-derived HC (previously carbonized at 1200 ℃) by an hydrothermal carbonization process [160].

3.4.2. Nanocomposites

Carbon materials can also be used as matrix for loading metallic nanoparticles (NPs) or other active materials. These composites can notably increase the electronic conductivity and the storage capacity of the HC. At the same time, the carbon framework buffers the high-volume changes during redox reactions at metal NPs. As a result, these advanced materials can provide higher reversible capacities, greater high-rate capabilities, and better cycling stability. NPs of Sb [168], Se [169], SnO_2 [170], CoP [171] and Cu_3P [172] have been used with different carbon materials, showing promising reversible capacities and high rate capabilities for SIBs.

In the last years, few composites from plant-derived HCs have been studied as SIB anodes. Ni NPs were embedded in a KOH-activated Loofah-derived HC by a simple hydrothermal treatment with $NiCl_2$, followed by an annealing step at 800 °C [173]. Conductivity of the resulting material was improved, since graphitic carbon was formed on the surface of metallic NPs, leading to a better reversible capacity and rate performance. Cheng et. al [174] studied the addition of FeS_2 NPs into a $Fe(NO_3)_3$-doped juncus biomass-derived carbon matrix via a pyrolysis step at 900 °C, followed by a second carbonization step at 500 °C in the presence of S. After 1000 galvanostatic cycles at a current density of 1 A g^{-1}, the synthetized nanocomposite exhibited a high capacity of 432 mA h g^{-1}. Su et al. [175] embedded $MoSe_2$ NPs and carbon nanotubes within a mangosteen epicarp-derived HC that was previously activated by KOH at 800 °C. The resulting composite delivered a capacity of 405 mA h g^{-1} after 250 cycles at 0.2 A g^{-1}.

The above-reported remarkable performances were surpassed by a red phosphorus/HC composite. Red phosphorus is a well-known anode candidate because of its high theoretical capacity of 2596 mA h g^{-1}. Unfortunately, its low conductivity and huge volume changes during sodiation/desodiation cycles prevent its use in SIBs. Tian et al. [176] made a coconut shell-derived HC/red phosphorus composite through a simple procedure. The biomass was activated with $ZnCl_2$ at 650 °C, then carbonized at 900 °C, and finally mixed with red phosphorus and heated again at 450 °C for 3 h. A phosphorus content of 53 wt% was measured

in the composite and, after 100 cycles, the composite exhibited a reversible capacity of 993 mA h g^{-1} at a current rate of 0.5 A g^{-1}, with a high ICE of 89 %.

Fig. 9 summarizes the electrochemical performance of doped HCs. Good or very good reversible capacities were obtained in all cases for both low (≤0.1 A g^{-1}) and high (1 A g^{-1}) current rates; being always significantly higher than those reported for HCs produced via nondoped activation procedures (see Fig. 6). Particularly noteworthy is the good performance of the N-S dual doped cotton-derived HC, as well as the already commented red P/HC composite. Surface redox reactions promoted in the doped HCs are faster than bulk intercalation reactions. This fact, together with low electrode structural changes upon cycling, contributes to the high rate capability and cycling stability [114,177]. It has also to point out that these advanced materials were produced at relatively low carbonization temperatures (500–900 °C).

4. Conclusion and prospects

In view of the need to replace lithium-ion batteries, sodium-ion batteries are the most promising candidates to implement large-scale energy storage systems. Great efforts have been made during the last years in terms of electrode materials and electrolyte formulations towards competitive SIBs. However, while cathode performance is close to that of the current Li-ion technology, further improvement for the anode should be done in terms of energy and power density, as well as cycling stability. Biomass-derived hard carbon is a promising anode material candidate due to its electrochemical performance at relatively low cost and environmental impact. In this article, we reviewed the fundamental and current knowledge about plant-derived HC anodes with the aim at providing researchers with the basic tools required to delve into this topic.

Dry and hydrothermal carbonization of plant-derived biomass are common thermochemical processing routes to prepare HCs. They represent cheaper and more sustainable approaches than synthetic routes involving fossil fuel-based precursors. The natural porous structures of plant precursors remain in the final carbon material, providing shorter diffusion paths for Na^+ and more storage sites to enhance the HC electrode capacity. By adjusting the carbonization temperature in the range of 1000–1400 °C (carbonization up to this highest temperature is usually conducted after preliminary pyrolysis or HCT steps), the microstructures of HC can be tailored to optimal specific surface area and interlayer spacing (0.38–0.40 nm) in order to reach the maximum coulombic efficiency and reversible storage of sodium. Biomass feedstock selection plays a key role in determining the properties of the resulting HCs and, therefore, the optimum highest carbonization temperature.

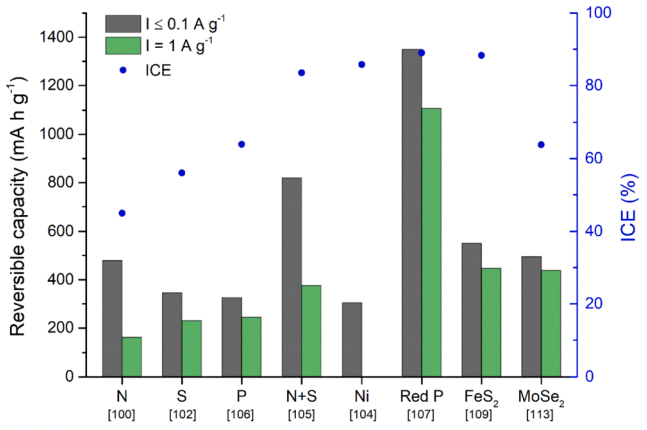

Fig. 9. Reversible capacities obtained for different doped plant-derived HC anodes in SIB half-cells at a current rate lower or equal than 0.1 and 1 A g^{-1}. More details are available in Table S5.

Nevertheless, despite the considerable progress made in the last years, there is still a long road ahead to reach the full potential of this technology. More research efforts should be focused on the following points (see Fig. 10):

(i) In-depth knowledge of Na storage mechanism. With regard to the sodium storage in HC, multiple mechanisms have been proposed in the last years. Nonetheless, the fact that an adsorption storage process is associated with the slope region and that an intercalation mechanism is linked to the plateau region is being accepted by an increasing number of researchers. The global mechanism, however, still remains inconclusive and needs to be further investigated, especially in terms of the low-voltage plateau, ultra-micropores, and closed pores filling. Further research —using in/ex situ techniques as well as theorical calculations and simulations— is required to better understand the role of pore size distribution, open and closed porosity, functional groups on surface, structural defects, and pseudographitic domains during sodiation/desodiation processes.

(ii) Rational structure design of anodes. To further improve the anode performance through tuning the porosity of HCs, physical and chemical activation processes are proposed. Hierarchical pore structures improve the interface wettability and the rate performance of the anode. Since Na^+ diffusion in the bulk of the carbon seems to be the rate-limiting step, an increased porosity can reduce the required Na^+ diffusion distances. Furthermore, despite the low ICE values as negative aspect, producing competitive carbons at temperatures below 1000 °C could be an advantage for their manufacturing at large scale. Other emerging strategies as microwave activation, H_2 reduction, and high current pretreatments have been also proposed and their suitability should be further assessed. The specific capacity and ICE of activated HCs can be improved by heteroatom doping. This approach could enhance the ionic conductivity, provide more active sites, and even enlarge the interlayer spacing. Furthermore, the synthesis of nanocomposites with metallic NPs (or allowing materials) begins to receive more attention since it seems to be able to produce SIB anodes having excellent reversible capacities and high-rate capabilities.

(iii) ICE improvement. Improving the ICE of HC electrodes is also a crucial task to enhance the energy density and enable SIBs to be produced and marketed. Low ICE is caused by a certain decomposition of the electrolyte and also by the irreversible sodium trapping in pores, functional groups, and interlayer spaces. Optimizing electrolyte and binder formulations, together with HC engineering of defects, surface area, and functional groups are interesting strategies to improve it. Nevertheless, a comprehensive knowledge on the formation and role of the SEI is crucial to facilitate a rational and efficient electrode design. Recently, chemically presodiation of the HC anodes before assembling the cell has been proposed as an effective and scalable alternative. Finally, the production of HCs with enhanced conductivity would allow, among other benefits, to reduce the amount of additive (usually carbon black) or even avoid it, also resulting in an improvement of the ICE.

(iv) Environmental, economic, and scaling-up aspects. One of the main strengths of plant-derived HCs —compared with synthetic materials— relates to the possibility of producing them via easily scalable processes at relatively low cost. This competitive advantage, however, could be further strengthened by implementing less energy-intensive processes and avoiding the use of expensive and/or hazardous chemicals. In this sense, synthesis of HCs at relatively mild temperatures via, for instance, heteroatom doping using cheap and sustainable sources (or even waste streams) is encouraged. This achievement could definitely boost SIBs technology and bring it closer to its commercialization.

(v) Full cell approach. The study of HC anodes in full cells, in which the cathode doesn't supply infinite Na ions, is required to evaluate their performance in a realistic situation. Several types of cathode materials have been developed and assembled in commercial SIBs (e.g., layered oxides, NVPF, and Prussian blue analogue cathodes assembled by Faradion, Tiamat, and Novasis, respectively [178,179]). Although some

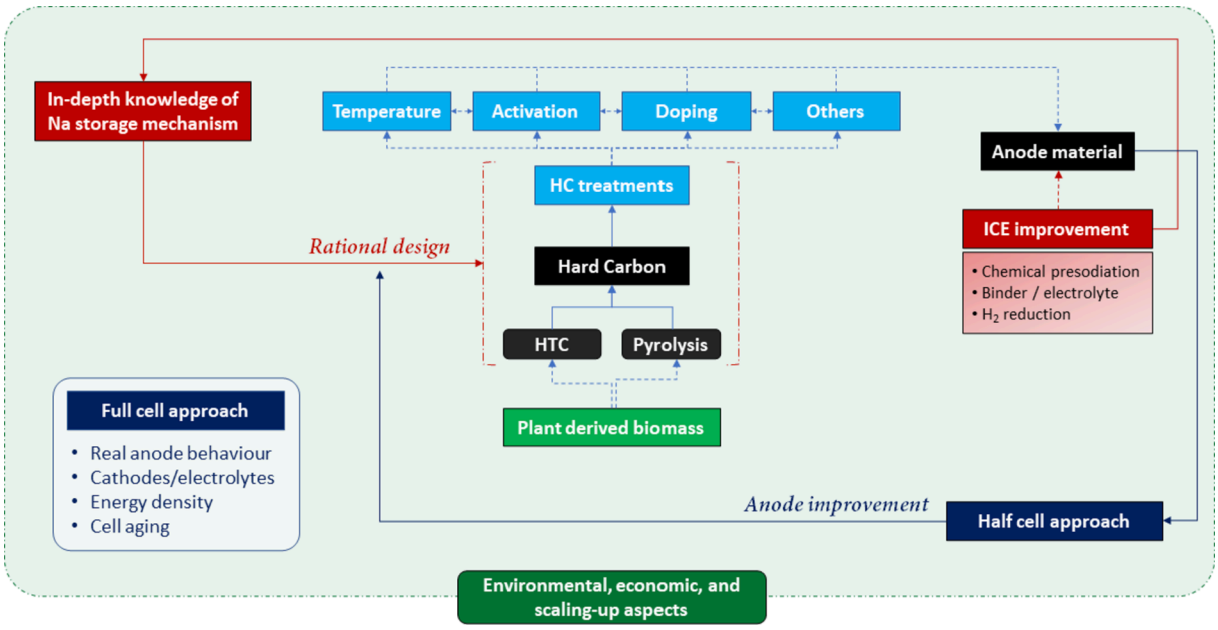

Fig. 10. Prospective challenges for improving the performance of plant-derived HCs as anodes in SIBs.

plant-derived HC anodes have been studied coupled with these cathodes, more full cell studies are necessary —particularly once the anode has been optimized— to check some issues that rarely are considered in half cells testing. Full cells are required to calculate the areal reversible capacity ratio of the negative to the positive electrode (N/P ratio), select the cut-off voltage, and check the polarizability of both electrodes, the aging of the cell, and the climate influence. Moreover, the compatibility of electrolytes and additives with the anode and cathode materials is particularly relevant. Regarding electrolytes, some additives (for instance, FEC) have been studied to improve the most used alkyl carbonate-based electrolytes in terms of cell ICE and cycling stability. Moreover, a growing number of studies revealed that using ether-based electrolytes results in the formation of more stable SEI films on HC anodes. Exploring those electrolytes, together with most advanced solid and gel-based electrolytes, could improve the anode and cell performances, not only affecting the SEI, but also increasing the voltage window of the full cell and, therefore, the energy density.

To conclude, easily tunable plant-derived HCs appear as suitable anode candidates for SIBs. To fit the properties of the anodes to the battery requirements, a combination of different processes can be applied thanks to synergistic effects. Thus, activation and doping strategies might efficiently be combined to reach an optimum balance between several parameters, including —but not limited to— ICE, energy density, and power density of the final electrodes. Particular effort has to be devoted to elucidate the impact of both the pore size distribution and the nature of the SEI film on the ICE, rate capability, and long-cycle stability. Once this necessary progress is achieved, sustainable, high-performance and low-cost HC-based anodes are expected to be produced from plant wastes in the near future to be assembled in large-scale energy storage systems.

Declaration of Competing Interest

The authors declare that they have no known competing financial interests or personal relationships that could have appeared to influence the work reported in this paper.

Acknowledgements

This work is part of the research project PID2019-107737RB-I00, funded by MCIN/AEI/10.13039/501100011033. The authors also acknowledge the funding from the Aragón Government (Ref. T22_20R), funded by FEDER 2014-2020 "Construyendo Europa desde Aragón". DA also acknowledges the funding from the Regional Government of Aragon (Spain) with a grant for postgraduate research contracts (2019-2023).

Appendix A. Supplementary data

Supplementary data to this article can be found online at https://doi.org/10.1016/j.cej.2022.137468.

References

[1] National Oceanic and Atmospheric Administration, Carbon dioxide peaks near 420 parts per million at Mauna Loa observatory, (2021). https://research.noaa.gov/article/ArtMID/587/Artic (accessed February 1, 2022).
[2] Meteorological office, Mauna Loa carbon dioxide forecast for 2022, (2022). https://www.metoffice.gov.uk/research/climate/seasonal-to-decadal/long-range/forecasts/co2-forecast (accessed February 1, 2022).
[3] B. Dunn, H. Kamath, J.-M. Tarascon, Electrical energy storage for the grid: a battery of choices, Science 334 (6058) (2011) 928–935.
[4] I. Tsiropoulos, D. Tarvydas, N. Lebedeva, Li-ion batteries for mobility and stationary storage applications, Luxembourg (2018), https://doi.org/10.2760/87175.
[5] G. Martin, L. Rentsch, M. Höck, M. Bertau, Lithium market research – global supply, future demand and price development, Energy Storage Mater. 6 (2017) 171–179, https://doi.org/10.1016/j.ensm.2016.11.004.
[6] European Commission, Critical Raw Materials Resilience: Charting a Path towards greater Security and Sustainability, Brussels, 2020.
[7] N.N. Greenwood, A. Earnshaw, Lithium, Sodium, Potassium, Rubidium, Caesium and Francium, in: Chem. Elem., Second Edi, Elsevier, 1997: pp. 68–106. https://doi.org/10.1016/B978-0-7506-3365-9.50010-9.
[8] R.S. Carmichael, Practical Handbook of Physical Properties of Rocks and Minerals (1988), CRC Press, 2017. https://doi.org/10.1201/9780203710968.
[9] J.M. Tarascon, Na-ion versus Li-ion batteries: complementarity rather than competitiveness, Joule 4 (2020) 1616–1620, https://doi.org/10.1016/j.joule.2020.06.003.
[10] M. Okoshi, Y. Yamada, S. Komaba, A. Yamada, H. Nakai, Theoretical analysis of interactions between potassium ions and organic electrolyte solvents: a comparison with lithium, sodium, and magnesium ions, J. Electrochem. Soc. 164 (2017) A54–A60, https://doi.org/10.1149/2.0211702jes.
[11] J.J. Braconnier, C. Delmas, C. Fouassier, P. Hagenmuller, Comportement electrochimique des phases $NaxCoO_2$, Mater. Res. Bull. 15 (1980) 1797–1804, https://doi.org/10.1016/0025-5408(80)90199-3.
[12] Y. Li, Y. Lu, C. Zhao, Y.S. Hu, M.M. Titirici, H. Li, X. Huang, L. Chen, Recent advances of electrode materials for low-cost sodium-ion batteries towards practical application for grid energy storage, Energy Storage Mater. 7 (2017) 130–151, https://doi.org/10.1016/j.ensm.2017.01.002.

[13] D.A. Stevens, J.R. Dahn, High capacity anode materials for rechargeable sodium-ion batteries, J. Electrochem. Soc. 147 (2000) 1271, https://doi.org/10.1149/1.1393348.

[14] H. Shi, J. Barker, M.Y. Saïdi, R. Koksbang, L. Morris, Graphite structure and lithium intercalation, J. Power Sources 68 (1997) 291–295, https://doi.org/10.1016/S0378-7753(96)02562-1.

[15] L. Jiang, L. Sheng, Z. Fan, Biomass-derived carbon materials with structural diversities and their applications in energy storage, Sci. China Mater. 61 (2) (2018) 133–158.

[16] A.J. Bard, G. Inzelt, F. Scholz, Electrochemical dictionary, Springer-Verlag Berlin Heidelberg, 2008. https://doi.org/10.1007/978-3-340-74598-3.

[17] S. Komaba, W. Murata, T. Ishikawa, N. Yabuuchi, T. Ozeki, T. Nakayama, A. Ogata, K. Gotoh, K. Fujiwara, Electrochemical Na insertion and solid electrolyte interphase for hard-carbon electrodes and application to Na-ion batteries, Adv. Funct. Mater. 21 (2011) 3859–3867, https://doi.org/10.1002/adfm.201100854.

[18] D. Linden, T.B. Reddy, Handbook of batteries, Third edit, McGraw-Hill, New York, Chicago, San Francisco, Lisbon, London, Madrid, Mexico City, Milan, New Delhi, San Juan, Seoul, Singapore, Sydney, Toronto, 2002.

[19] K. Kubota, M. Dahbi, T. Hosaka, S. Kumakura, S. Komaba, Towards K-Ion and Na-Ion Batteries as "Beyond Li-Ion", Chem. Rec. 18 (2018) 459–479, https://doi.org/10.1002/tcr.201700057.

[20] Z. Jian, W. Luo, X. Ji, Carbon electrodes for K-Ion batteries, J. Am. Chem. Soc. 137 (2015) 11566–11569, https://doi.org/10.1021/jacs.5b06809.

[21] S. Komaba, T. Hasegawa, M. Dahbi, K. Kubota, Potassium intercalation into graphite to realize high-voltage/high-power potassium-ion batteries and potassium-ion capacitors, Electrochem. Commun. 60 (2015) 172–175, https://doi.org/10.1016/j.elecom.2015.09.002.

[22] D.A. Stevens, J.R. Dahn, The mechanisms of lithium and sodium insertion in carbon materials, J. Electrochem. Soc. 148 (2001) A803, https://doi.org/10.1149/1.1379565.

[23] R.C. Asher, A lamellar compound of sodium and graphite, J. Inorg. Nucl. Chem. 10 (1959) 238–249, https://doi.org/10.1016/0022-1902(59)80118-4.

[24] Y. Li, Y. Lu, P. Adelhelm, M.M. Titirici, Y.S. Hu, Intercalation chemistry of graphite: alkali metal ions and beyond, Chem. Soc. Rev. 48 (2019) 4655–4687, https://doi.org/10.1039/c9cs00162j.

[25] D.P. Divincenzo, E.J. Mele, Cohesion and structure in stage-1 graphite intercalation compounds, Phys. Rev. B. 32 (1985) 2538–2553, https://doi.org/10.1103/PhysRevB.32.2538.

[26] O. Lenchuk, P. Adelhelm, D. Mollenhauer, New insights into the origin of unstable sodium graphite intercalation compounds, Phys. Chem. Chem. Phys. 21 (2019) 19378–19390, https://doi.org/10.1039/c9cp03453f.

[27] S. Rubio, R.R. Maça, M.J. Aragón, M. Cabello, M. Castillo-Rodríguez, P. Lavela, J. L. Tirado, V. Etacheri, G.F. Ortiz, Superior electrochemical performance of TiO_2 sodium-ion battery anodes in diglyme-based electrolyte solution, J. Power Sources. 432 (2019) 82–91, https://doi.org/10.1016/j.jpowsour.2019.05.070.

[28] J. Huo, Y. Ren, G. Zhang, X. Wang, S. Guo, Boosting sodium storage of hierarchical nanofibers with porous carbon-supported anatase TiO_2/TiO_2(B) nanowires, ACS Appl. Energy Mater. 5 (2022) 3447–3453, https://doi.org/10.1021/acsaem.1c04018.

[29] R.E. Franklin, Crystallite growth in graphitizing and non-graphitizing carbons, Proc. R. Soc. London. Ser. A. Math. Phys. Sci. 209 (1951) 196–218, https://doi.org/10.1098/rspa.1951.0197.

[30] H. Azuma, H. Imoto, S.N.I. Yamada, K. Sekai, Advanced carbon anode materials for lithium ion cells, J. Power Sources. 81–82 (1999) 1–7, https://doi.org/10.1016/S0378-7753(99)00122-6.

[31] M. Song, C. Wang, D. Du, F. Li, J. Chen, A high-energy-density sodium-ion full battery based on tin anode, Sci. China Chem. 62 (2019) 616–621, https://doi.org/10.1007/s11426-018-9422-y.

[32] H. Lu, L. Wu, L. Xiao, X. Ai, H. Yang, Y. Cao, Investigation of the effect of fluoroethylene carbonate additive on electrochemical performance of sb-based anode for sodium-ion batteries, Electrochim. Acta 190 (2016) 402–408, https://doi.org/10.1016/j.electacta.2015.12.136.

[33] M. Dahbi, N. Yabuuchi, M. Fukunishi, K. Kubota, K. Chihara, K. Tokiwa, X.F. Yu, H. Ushiyama, K. Yamashita, J.Y. Son, Y.T. Cui, H. Oji, S. Komaba, Black phosphorus as a high-capacity, high-capability negative electrode for sodium-ion batteries: investigation of the electrode/electrolyte interface, Chem. Mater. 28 (2016) 1625–1635, https://doi.org/10.1021/acs.chemmater.5b03524.

[34] S. Fang, D. Bresser, S. Passerini, Transition metal oxide anodes for electrochemical energy storage in lithium- and sodium-ion batteries, Adv. Energy Mater. 10 (1) (2020) 1902485.

[35] J. Wu, S. Liu, Y. Rehman, T. Huang, J. Zhao, Q. Gu, J. Mao, Z. Guo, Phase engineering of nickel sulfides to boost sodium- and potassium-ion storage performance, Adv. Funct. Mater. 31 (2021) 2010832, https://doi.org/10.1002/adfm.202010832.

[36] P. Zhou, M. Zhang, L. Wang, Q. Huang, Z. Su, L. Li, X. Wang, Y. Li, C. Zeng, Z. Guo, Synthesis and electrochemical performance of ZnSe electrospinning nanofibers as an anode material for lithium ion and sodium ion batteries, Front. Chem. 7 (2019) 1–10, https://doi.org/10.3389/fchem.2019.00569.

[37] H. Kang, Y. Liu, K. Cao, Y. Zhao, L. Jiao, Y. Wang, H. Yuan, Update on anode materials for Na-ion batteries, J. Mater. Chem. A. 3 (2015) 17899–17913, https://doi.org/10.1039/c5ta03181h.

[38] F. Klein, B. Jache, A. Bhide, P. Adelhelm, Conversion reactions for sodium-ion batteries, Phys. Chem. Chem. Phys. 15 (2013) 15876–15887, https://doi.org/10.1039/c3cp52125g.

[39] J. Górka, C. Vix-Guterl, C. Matei Ghimbeu, Recent progress in design of biomass-derived hard carbons for sodium ion batteries, C. 2 (2016) 24, https://doi.org/10.3390/c2040024.

[40] Y. Liu, J.S. Xue, T. Zheng, J.R. Dahn, Mechanism of lithium insertion in hard carbons prepared by pyrolysis of epoxy resins, Carbon N. Y. 34 (1996) 193–200, https://doi.org/10.1016/0008-6223(96)00177-7.

[41] M. Dahbi, M. Kiso, K. Kubota, T. Horiba, T. Chafik, K. Hida, T. Matsuyama, S. Komaba, Synthesis of hard carbon from argan shells for Na-ion batteries, J. Mater. Chem. A. 5 (2017) 9917–9928, https://doi.org/10.1039/c7ta01394a.

[42] Y. Cao, L. Xiao, M.L. Sushko, W. Wang, B. Schwenzer, J. Xiao, Z. Nie, L.V. Saraf, Z. Yang, J. Liu, Sodium ion insertion in hollow carbon nanowires for battery applications, Nano Lett. 12 (2012) 3783–3787, https://doi.org/10.1021/nl3016957.

[43] J. Ding, H. Wang, Z. Li, A. Kohandehghan, K. Cui, Z. Xu, B. Zahiri, X. Tan, E. M. Lotfabad, B.C. Olsen, D. Mitlin, Carbon nanosheet frameworks derived from peat moss as high performance sodium ion battery anodes, ACS Nano. 7 (2013) 11004–11015, https://doi.org/10.1021/nn404640c.

[44] N. Zhang, Q. Liu, W. Chen, M. Wan, X. Li, L. Wang, L. Xue, W. Zhang, High capacity hard carbon derived from lotus stem as anode for sodium ion batteries, J. Power Sources 378 (2018) 331–337, https://doi.org/10.1016/j.jpowsour.2017.12.054.

[45] C. Bommier, T.W. Surta, M. Dolgos, X. Ji, New mechanistic insights on Na-Ion storage in nongraphitizable carbon, Nano Lett. 15 (2015) 5888–5892, https://doi.org/10.1021/acs.nanolett.5b01969.

[46] Y. Morikawa, S.-I. Nishimura, R.-I. Hashimoto, M. Ohnuma, A. Yamada, Mechanism of sodium storage in hard carbon: an X-Ray scattering analysis, Adv. Energy Mater. 10 (3) (2020) 1903176.

[47] X. Yin, Z. Lu, J. Wang, X. Feng, S. Roy, X. Liu, Y. Yang, Y. Zhao, J. Zhang, Enabling fast Na+ transfer kinetics in the whole-voltage-region of hard-carbon anodes for ultrahigh-rate sodium storage, Adv. Mater. 34 (2022) 2109282, https://doi.org/10.1002/adma.202109282.

[48] X. Yin, Y. Zhao, X. Wang, X. Feng, Z. Lu, Y. Li, H. Long, J. Wang, J. Ning, J. Zhang, Modulating the graphitic domains of hard carbons derived from mixed pitch and resin to achieve high rate and stable sodium storage, Small 18 (2022) 1–11, https://doi.org/10.1002/smll.202105568.

[49] S. Alvin, D. Yoon, C. Chandra, H.S. Cahyadi, J.H. Park, W. Chang, K.Y. Chung, J. Kim, Revealing sodium ion storage mechanism in hard carbon, Carbon N. Y. 145 (2019) 67–81, https://doi.org/10.1016/j.carbon.2018.12.112.

[50] N. Sun, Z. Guan, Y. Liu, Y. Cao, Q. Zhu, H. Liu, Z. Wang, P. Zhang, B. Xu, Extended "Adsorption–Insertion" Model: a new insight into the sodium storage mechanism of hard carbons, Adv. Energy Mater. 9 (2019) 1–14, https://doi.org/10.1002/aenm.201901351.

[51] B. Zhang, C.M. Ghimbeu, C. Laberty, C. Vix-Guterl, J.M. Tarascon, Correlation between microstructure and na storage behavior in hard carbon, Adv. Energy Mater. 6 (2016) 1–9, https://doi.org/10.1002/aenm.201501588.

[52] Y. Li, Y.S. Hu, M.M. Titirici, L. Chen, X. Huang, Hard carbon microtubes made from renewable cotton as high-performance anode material for sodium-ion batteries, Adv. Energy Mater. 6 (2016) 1–9, https://doi.org/10.1002/aenm.201600659.

[53] P. Bai, Y. He, X. Zou, X. Zhao, P. Xiong, Y. Xu, Elucidation of the sodium-storage mechanism in hard carbons, Adv. Energy Mater. 8 (2018) 1–9, https://doi.org/10.1002/aenm.201703217.

[54] X. Meng, P.E. Savage, D. Deng, Trash to treasure: from harmful algal blooms to high-performance electrodes for sodium-ion batteries, Environ. Sci. Technol. 49 (2015) 12543–12550, https://doi.org/10.1021/acs.est.5b03882.

[55] M. Yan, Y. Qin, L. Wang, M. Song, D. Han, Q. Jin, S. Zhao, M. Zhao, Z. Li, X. Wang, L. Meng, X. Wang, Recent advances in biomass-derived carbon materials for sodium-ion energy storage devices, Nanomaterials. 12 (6) (2022) 930.

[56] D. Li, L. Zhang, H. Chen, L.X. Ding, S. Wang, H. Wang, Nitrogen-doped bamboo-like carbon nanotubes: promising anode materials for sodium-ion batteries, Chem. Commun. 51 (2015) 16045–16048, https://doi.org/10.1039/c5cc06266g.

[57] Z.E. Yu, Y. Lyu, Y. Wang, S. Xu, H. Cheng, X. Mu, J. Chu, R. Chen, Y. Liu, B. Guo, Hard carbon micro-nano tubes derived from kapok fiber as anode materials for sodium-ion batteries and the sodium-ion storage mechanism, Chem. Commun. 56 (2020) 778–781, https://doi.org/10.1039/c9cc08221b.

[58] Z. Zhu, F. Liang, Z. Zhou, X. Zeng, D. Wang, P. Dong, J. Zhao, S. Sun, Y. Zhang, X. Li, Expanded biomass-derived hard carbon with ultra-stable performance in sodium-ion batteries, J. Mater. Chem. A. 6 (2018) 1513–1522, https://doi.org/10.1039/c7ta07951f.

[59] C. Li, J. Li, Y. Zhang, X. Cui, H. Lei, G. Li, Heteroatom-doped hierarchically porous carbons derived from cucumber stem as high-performance anodes for sodium-ion batteries, J. Mater. Sci. 54 (2019) 5641–5657, https://doi.org/10.1007/s10853-018-03229-2.

[60] Y.-M. Chang, H.-W. Lin, L.-J. Li, H.-Y. Chen, Two-dimensional materials as anodes for sodium-ion batteries, Mater. Today Adv. 6 (2020) 100054.

[61] Y. Zhang, X. Li, P. Dong, G. Wu, J. Xiao, X. Zeng, Y. Zhang, X. Sun, Honeycomb-like hard carbon derived from pine pollen as high-performance anode material for sodium-ion batteries, ACS Appl. Mater. Interfaces. 10 (2018) 42796–42803, https://doi.org/10.1021/acsami.8b13160.

[62] D. Qin, S. Chen, A sustainable synthesis of biomass carbon sheets as excellent performance sodium ion batteries anode, J. Solid State Electrochem. 21 (2017) 1305–1312, https://doi.org/10.1007/s10008-016-3485-z.

[63] Y. Zheng, Y. Lu, X. Qi, Y. Wang, L. Mu, Y. Li, Q. Ma, J. Li, Y.S. Hu, Superior electrochemical performance of sodium-ion full-cell using poplar wood derived hard carbon anode, Energy Storage Mater. 18 (2019) 269–279, https://doi.org/10.1016/j.ensm.2018.09.002.

[64] Y. Li, Y. Lu, Q. Meng, A.C.S. Jensen, Q. Zhang, Q. Zhang, Y. Tong, Y. Qi, L. Gu, M.-M. Titirici, Y.-S. Hu, Regulating pore structure of hierarchical porous waste cork-derived hard carbon anode for enhanced Na storage performance, Adv. Energy Mater. 9 (48) (2019) 1902852.

[65] Y. Zhu, M. Chen, Q. Li, C. Yuan, C. Wang, A porous biomass-derived anode for high-performance sodium-ion batteries, Carbon N. Y. 129 (2018) 695–701, https://doi.org/10.1016/j.carbon.2017.12.103.

[66] J. Zhu, Y. Shan, T. Wang, H. Sun, Z. Zhao, L. Mei, Z. Fan, Z. Xu, I. Shakir, Y. Huang, B. Lu, X. Duan, A hyperaccumulation pathway to three-dimensional hierarchical porous nanocomposites for highly robust high-power electrodes, Nat. Commun. 7 (2016) 1–10, https://doi.org/10.1038/ncomms13432.

[67] X. Dou, I. Hasa, M. Hekmatfar, T. Diemant, R.J. Behm, D. Buchholz, S. Passerini, Pectin, Hemicellulose, or Lignin? Impact of the biowaste source on the performance of hard carbons for sodium-ion batteries, ChemSusChem 10 (2017) 2668–2676, https://doi.org/10.1002/cssc.201700628.

[68] L.J. Gibson, The hierarchical structure and mechanics of plant materials, J. R. Soc. Interface 9 (2012) 2749–2766, https://doi.org/10.1098/rsif.2012.0341.

[69] K. Wang, K.H. Kim, R.C. Brown, Catalytic pyrolysis of individual components of lignocellulosic biomass, Green Chem. 16 (2014) 727–735, https://doi.org/10.1039/c3gc41288a.

[70] K. Açıkalın, Pyrolytic characteristics and kinetics of pistachio shell by thermogravimetric analysis, J. Therm. Anal. Calorim. 109 (2012) 227–235, https://doi.org/10.1007/s10973-011-1714-3.

[71] J. Deng, T. Xiong, H. Wang, A. Zheng, Y. Wang, Effects of cellulose, hemicellulose, and lignin on the structure and morphology of porous carbons, ACS Sustain. Chem. Eng. 4 (2016) 3750–3756, https://doi.org/10.1021/acssuschemeng.6b00388.

[72] C.D.M. Saavedra Rios, V. Simone, L. Simonin, S. Martinet, C. Dupont, Biochars from various biomass types as precursors for hard carbon anodes in sodium-ion batteries, Biomass Bioenergy 117 (2018) 32–37.

[73] E.M. Lotfabad, J. Ding, K. Cui, A. Kohandehghan, W.P. Kalisvaart, M. Hazelton, D. Mitlin, High-density sodium and lithium ion battery anodes from banana peels, ACS Nano 8 (2014) 7115–7129, https://doi.org/10.1021/nn502045y.

[74] M. Poletto, A.J. Zattera, M.M.C. Forte, R.M.C. Santana, Thermal decomposition of wood: Influence of wood components and cellulose crystallite size, Bioresour. Technol. 109 (2012) 148–153, https://doi.org/10.1016/j.biortech.2011.11.122.

[75] P.C. Rath, J. Patra, H.T. Huang, D. Bresser, T.Y. Wu, J.K. Chang, Carbonaceous anodes derived from sugarcane bagasse for sodium-ion batteries, ChemSusChem 12 (2019) 2302–2309, https://doi.org/10.1002/cssc.201900319.

[76] C.D.M. Saavedra Rios, L. Simonin, A.d. Geyer, C. Matei Ghimbeu, C. Dupont, Unraveling the properties of biomass-derived hard carbons upon thermal treatment for a practical application in Na-Ion batteries, Energies 13 (14) (2020) 3513.

[77] J.J. Manyà, Pyrolysis for biochar purposes: a review to establish current knowledge gaps and research needs, Environ. Sci. Technol. 46 (2012) 7939–7954, https://doi.org/10.1021/es301029g.

[78] W.J. Liu, H. Jiang, H.Q. Yu, Development of biochar-based functional materials: toward a sustainable platform carbon material, Chem. Rev. 115 (2015) 12251–12285, https://doi.org/10.1021/acs.chemrev.5b00195.

[79] W.J. Liu, H. Jiang, H.Q. Yu, Emerging applications of biochar-based materials for energy storage and conversion, Energy Environ. Sci. 12 (2019) 1751–1779, https://doi.org/10.1039/c9ee00206e.

[80] T. Zhang, J. Mao, X. Liu, M. Xuan, K. Bi, X.L. Zhang, J. Hu, J. Fan, S. Chen, G. Shao, Pinecone biomass-derived hard carbon anodes for high-performance sodium-ion batteries, RSC Adv. 7 (2017) 41504–41511, https://doi.org/10.1039/c7ra07231g.

[81] V. Simone, A. Boulineau, A. de Geyer, D. Rouchon, L. Simonin, S. Martinet, Hard carbon derived from cellulose as anode for sodium ion batteries: dependence of electrochemical properties on structure, J. Energy Chem. 25 (2016) 761–768, https://doi.org/10.1016/j.jechem.2016.04.016.

[82] S. Alvin, D. Yoon, C. Chandra, R.F. Susanti, W. Chang, C. Ryu, J. Kim, Extended flat voltage profile of hard carbon synthesized using a two-step carbonization approach as an anode in sodium ion batteries, J. Power Sources 430 (2019) 157–168, https://doi.org/10.1016/j.jpowsour.2019.05.013.

[83] C. Marino, J. Cabanero, M. Povia, C. Villevieille, Biowaste lignin-based carbonaceous materials as anodes for Na-ion batteries, J. Electrochem. Soc. 165 (2018) A1400–A1408, https://doi.org/10.1149/2.0681807jes.

[84] Z. Xu, J. Chen, M. Wu, C. Chen, Y. Song, Y. Wang, Effects of different atmosphere on electrochemical performance of hard carbon electrode in sodium ion battery, Electron. Mater. Lett. 15 (2019) 428–436, https://doi.org/10.1007/s13391-019-00143-w.

[85] E. Irisarri, A. Ponrouch, M.R. Palacin, Review—hard carbon negative electrode materials for sodium-ion batteries, J. Electrochem. Soc. 162 (2015) A2476–A2482, https://doi.org/10.1149/2.0091514jes.

[86] L. Xiao, H. Lu, Y. Fang, M.L. Sushko, Y. Cao, X. Ai, H. Yang, J. Liu, Low-defect and low-porosity hard carbon with high coulombic efficiency and high capacity for practical sodium ion battery anode, Adv. Energy Mater. 8 (2018) 1–7, https://doi.org/10.1002/aenm.201703238.

[87] A. Funke, F. Ziegler, Hydrothermal carbonization of biomass: a summary and discussion of chemical mechanisms for process engineering, Biofuels Bioprod. Biorefining 4 (2010) 160–177, https://doi.org/10.1002/bbb.198.

[88] Z. Gao, Y. Zhang, N. Song, X. Li, Biomass-derived renewable carbon materials for electrochemical energy storage, Mater. Res. Lett. 5 (2017) 69–88, https://doi.org/10.1080/21663831.2016.1250834.

[89] P. Zheng, T. Liu, X. Yuan, L. Zhang, Y. Liu, J. Huang, S. Guo, Enhanced performance by enlarged nano-pores of holly leaf-derived lamellar carbon for sodium-ion battery anode, Sci. Rep. 6 (2016) 1–9, https://doi.org/10.1038/srep26246.

[90] J. Wang, L. Yan, Q. Ren, L. Fan, F. Zhang, Z. Shi, Facile hydrothermal treatment route of reed straw-derived hard carbon for high performance sodium ion battery, Electrochim. Acta 291 (2018) 188–196, https://doi.org/10.1016/j.electacta.2018.08.136.

[91] K. Tang, L. Fu, R.J. White, L. Yu, M.M. Titirici, M. Antonietti, J. Maier, Hollow carbon nanospheres with superior rate capability for sodium-based batteries, Adv. Energy Mater. 2 (2012) 873–877, https://doi.org/10.1002/aenm.201100691.

[92] R. Li, J. Huang, Z. Xu, H. Qi, L. Cao, Y. Liu, W. Li, J. Li, Controlling the thickness of disordered turbostratic nanodomains in hard carbon with enhanced sodium storage performance, Energy Technol. 6 (2018) 1080–1087, https://doi.org/10.1002/ente.201700674.

[93] A. Anca-Couce, Reaction mechanisms and multi-scale modelling of lignocellulosic biomass pyrolysis, Prog. Energy Combust. Sci. 53 (2016) 41–79, https://doi.org/10.1016/j.pecs.2015.10.002.

[94] K. Kim, D.G. Lim, C.W. Han, S. Osswald, V. Ortalan, J.P. Youngblood, V.G. Pol, Tailored carbon anodes derived from biomass for sodium-ion storage, ACS Sustain. Chem. Eng. 5 (2017) 8720–8728, https://doi.org/10.1021/acssuschemeng.7b01497.

[95] N. Sun, H. Liu, B. Xu, Facile synthesis of high performance hard carbon anode materials for sodium ion batteries, J. Mater. Chem. A. 3 (2015) 20560–20566, https://doi.org/10.1039/c5ta05118e.

[96] P. Yu, W. Tang, F.F. Wu, C. Zhang, H.Y. Luo, H. Liu, Z.G. Wang, Recent progress in plant-derived hard carbon anode materials for sodium-ion batteries: a review, Rare Met. 39 (2020) 1019–1033, https://doi.org/10.1007/s12598-020-01443-z.

[97] J. Yang, X. Wang, W. Dai, X. Lian, X. Cui, W. Zhang, K. Zhang, M. Lin, R. Zou, K. P. Loh, Q.H. Yang, W. Chen, From micropores to ultra-micropores inside hard carbon: toward enhanced capacity in room-/low-temperature sodium-ion storage, Nano-Micro Lett. 13 (2021) 1–14, https://doi.org/10.1007/s40820-020-00587-y.

[98] X. Dou, C. Geng, D. Buchholz, S. Passerini, Research update: hard carbon with closed pores from pectin-free apple pomace waste for Na-ion batteries, APL Mater. 6 (4) (2018) 047501.

[99] M.E. Lee, H.W. Kwak, H.J. Jin, Y.S. Yun, Waste beverage coffee-induced hard carbon granules for sodium-ion batteries, ACS Sustain. Chem. Eng. 7 (2019) 12734–12740, https://doi.org/10.1021/acssuschemeng.9b00971.

[100] Y. Chen, Y. Wang, S. Zhu, K. Fu, X. Han, Y. Wang, B. Zhao, T. Li, B. Liu, Y. Li, J. Dai, H. Xie, T. Li, J.W. Connell, Y. Lin, L. Hu, Nanomanufacturing of graphene nanosheets through nano-hole opening and closing, Mater. Today 24 (2019) 26–32, https://doi.org/10.1016/j.mattod.2018.09.001.

[101] A. Karatrantos, Q. Cai, Effects of pore size and surface charge on Na ion storage in carbon nanopores, Phys. Chem. Chem. Phys. 18 (2016) 30761–30769, https://doi.org/10.1039/c6cp04611h.

[102] W. Li, J. Huang, L. Feng, L. Cao, Y. Ren, R. Li, Z. Xu, J. Li, C. Yao, Controlled synthesis of macroscopic three-dimensional hollow reticulate hard carbon as long-life anode materials for Na-ion batteries, J. Alloys Compd. 716 (2017) 210–219, https://doi.org/10.1016/j.jallcom.2017.05.062.

[103] A. Raj K, M.R. Panda, D.P. Dutta, S. Mitra, Bio-derived mesoporous disordered carbon: An excellent anode in sodium-ion battery and full-cell lab prototype, Carbon N. Y. 143 (2019) 402–412.

[104] X.K. Wang, J. Shi, L.W. Mi, Y.P. Zhai, J.Y. Zhang, X.M. Feng, Z.J. Wu, W.H. Chen, Hierarchical porous hard carbon enables integral solid electrolyte interphase as robust anode for sodium-ion batteries, Rare Met. 39 (2020) 1053–1062, https://doi.org/10.1007/s12598-020-01469-3.

[105] E.M. Lotfabad, P. Kalisvaart, A. Kohandehghan, D. Karpuzov, D. Mitlin, Origin of non-SEI related coulombic efficiency loss in carbons tested against Na and Li, J. Mater. Chem. A. 2 (2014) 19685–19695, https://doi.org/10.1039/c4ta04995k.

[106] A.C.S. Jensen, E. Olsson, H. Au, H. Alptekin, Z. Yang, S. Cottrell, K. Yokoyama, Q. Cai, M.M. Titirici, A.J. Drew, Local mobility in electrochemically inactive sodium in hard carbon anodes after the first cycle, J. Mater. Chem. A. 8 (2020) 743–749, https://doi.org/10.1039/c9ta10113f.

[107] C. Correa, A. Kruse, Biobased functional carbon materials: production, characterization, and applications-A review, Materials (Basel) 11 (9) (2018) 1568.

[108] W. Chen, M. Gong, K. Li, M. Xia, Z. Chen, H. Xiao, Y. Fang, Y. Chen, H. Yang, H. Chen, Insight into KOH activation mechanism during biomass pyrolysis: chemical reactions between O-containing groups and KOH, Appl. Energy 278 (2020), 115730, https://doi.org/10.1016/j.apenergy.2020.115730.

[109] W. Yu, H. Wang, S. Liu, N. Mao, X. Liu, J. Shi, W. Liu, S. Chen, X. Wang, N, O-codoped hierarchical porous carbons derived from algae for high-capacity supercapacitors and battery anodes, J. Mater. Chem. A. 4 (2016) 5973–5983, https://doi.org/10.1039/c6ta01821a.

[110] T. Liu, X. Li, Biomass-derived nanostructured porous carbons for sodium ion batteries: a review, Mater. Technol. 34 (2019) 232–245, https://doi.org/10.1080/10667857.2018.1545392.

[111] A. Pozio, A. Aurora, P.P. Prosini, Hard carbon for sodium batteries: wood precursors and activation with first group hydroxide, J. Power Sources. 449 (2020), 227555, https://doi.org/10.1016/j.jpowsour.2019.227555.

[112] H. Wang, W. Yu, J. Shi, N. Mao, S. Chen, W. Liu, Biomass derived hierarchical porous carbons as high-performance anodes for sodium-ion batteries, Electrochim. Acta 188 (2016) 103–110, https://doi.org/10.1016/j.electacta.2015.12.002.

[113] Q. Li, J. Huang, L. Cao, J. He, Y. Wang, W. Wu, Y. He, J. Li, Revealing the sodium storage of surface C=O structure in high performance Na-ion battery, J. Electroanal. Chem. 854 (2019), 113554, https://doi.org/10.1016/j.jelechem.2019.113554.

[114] R. Li, J. Huang, W. Li, J. Li, L. Cao, Z. Xu, Y. He, A. Yu, G. Lu, Controlling carbon-oxygen double bond and pseudographic structure in shaddock peel derived hard carbon for enhanced sodium storage properties, Electrochim. Acta 313 (2019) 109–115, https://doi.org/10.1016/j.electacta.2019.04.166.
[115] K.L. Hong, L. Qie, R. Zeng, Z.Q. Yi, W. Zhang, D. Wang, W. Yin, C. Wu, Q.J. Fan, W.X. Zhang, Y.H. Huang, Biomass derived hard carbon used as a high performance anode material for sodium ion batteries, J. Mater. Chem. A. 2 (2014) 12733–12738, https://doi.org/10.1039/c4ta02068e.
[116] Z. Xu, Y. Huang, L. Ding, J. Huang, H. Gao, T. Li, Highly stable basswood porous carbon anode activated by phosphoric acid for a sodium ion battery, Energy Fuels 34 (2020) 11565–11573, https://doi.org/10.1021/acs.energyfuels.0c02286.
[117] X. Dou, I. Hasa, D. Saurel, M. Jauregui, D. Buchholz, T. Rojo, S. Passerini, Impact of the acid treatment on lignocellulosic biomass hard carbon for sodium-ion battery anodes, ChemSusChem 11 (2018) 3276–3285, https://doi.org/10.1002/cssc.201801148.
[118] R. Chen, L. Li, Z. Liu, M. Lu, C. Wang, H. Li, W. Ma, S. Wang, Preparation and characterization of activated carbons from tobacco stem by chemical activation, J. Air Waste Manag. Assoc. 67 (2017) 713–724, https://doi.org/10.1080/10962247.2017.1280560.
[119] Z. Yu, Z. Zhao, T. Peng, Coralloid carbon material based on biomass as a promising anode material for lithium and sodium storage, New J. Chem. 45 (2021) 7138–7144, https://doi.org/10.1039/d0nj01769h.
[120] C.C. Wang, W.L. Su, Understanding acid pretreatment of lotus leaves to prepare hard carbons as anodes for sodium ion batteries, Surf. Coatings Technol. 415 (2021), 127125, https://doi.org/10.1016/j.surfcoat.2021.127125.
[121] H. Fu, Z. Xu, R. Li, W. Guan, K. Yao, J. Huang, J. Yang, X. Shen, Network carbon with macropores from apple pomace for stable and high areal capacity of sodium storage, ACS Sustain. Chem. Eng. 6 (2018) 14751–14758, https://doi.org/10.1021/acssuschemeng.8b03297.
[122] S.D. Xu, Y. Zhao, S. Liu, X. Ren, L. Chen, W. Shi, X. Wang, D. Zhang, Curly hard carbon derived from pistachio shells as high-performance anode materials for sodium-ion batteries, J. Mater. Sci. 53 (2018) 12334–12351, https://doi.org/10.1007/s10853-018-2472-4.
[123] C. Chen, Y. Huang, Y. Zhu, Z. Zhang, Z. Guang, Z. Meng, P. Liu, Nonignorable influence of oxygen in hard carbon for sodium ion storage, ACS Sustain. Chem. Eng. 8 (2020) 1497–1506, https://doi.org/10.1021/acssuschemeng.9b05948.
[124] W. Shao, F. Hu, T. Zhang, S. Liu, C. Song, N. Li, Z. Weng, J. Wang, X. Jian, Engineering ultramicroporous carbon with abundant C═O as extended "slope-dominated" sodium ion battery anodes, ACS Sustain. Chem. Eng. 9 (2021) 9727–9739, https://doi.org/10.1021/acssuschemeng.1c01885.
[125] L. Yang, M. Hu, H. Zhang, W. Yang, R. Lv, Pore structure regulation of hard carbon: towards fast and high-capacity sodium-ion storage, J. Colloid Interface Sci. 566 (2020) 257–264, https://doi.org/10.1016/j.jcis.2020.01.085.
[126] T.K. Kumaresan, S.A. Masilamani, K. Raman, S.Z. Karazhanov, R. Subashchandrabose, High performance sodium-ion battery anode using biomass derived hard carbon with engineered defective sites, Electrochim. Acta 368 (2021), 137574, https://doi.org/10.1016/j.electacta.2020.137574.
[127] P. Wang, B. Qiao, Y. Du, Y. Li, X. Zhou, Z. Dai, J. Bao, Fluorine-doped carbon particles derived from lotus petioles as high-performance anode materials for sodium-ion batteries, J. Phys. Chem. C. 119 (2015) 21336–21344, https://doi.org/10.1021/acs.jpcc.5b05443.
[128] D. Li, Y. Zhu, E. Xu, H. Wang, T. Chen, J. Quan, Y. Zhang, L. Wang, Y. Jiang, Ion- and air-tailored micro-honeycomb structures for superior Na-ion storage in coir-derived hard carbon, New J. Chem. 43 (2019) 10449–10457, https://doi.org/10.1039/c9nj01397k.
[129] K. Yu, X. Wang, H. Yang, Y. Bai, C. Wu, Insight to defects regulation on sugarcane waste-derived hard carbon anode for sodium-ion batteries, J. Energy Chem. 55 (2021) 499–508, https://doi.org/10.1016/j.jechem.2020.07.025.
[130] P. Wang, K. Zhu, K. Ye, Z. Gong, R. Liu, K. Cheng, G. Wang, J. Yan, D. Cao, Three-dimensional biomass derived hard carbon with reconstructed surface as a free-standing anode for sodium-ion batteries, J. Colloid Interface Sci. 561 (2020) 203–210, https://doi.org/10.1016/j.jcis.2019.11.091.
[131] L.F. Zhao, Z. Hu, W.H. Lai, Y. Tao, J. Peng, Z.C. Miao, Y.X. Wang, S.L. Chou, H. K. Liu, S.X. Dou, Hard carbon anodes: fundamental understanding and commercial perspectives for Na-Ion batteries beyond Li-Ion and K-Ion counterparts, Adv. Energy Mater. 11 (2021) 1–28, https://doi.org/10.1002/aenm.202002704.
[132] B. Xiao, F.A. Soto, M. Gu, K.S. Han, J. Song, H. Wang, M.H. Engelhard, V. Murugesan, K.T. Mueller, D. Reed, V.L. Sprenkle, P.B. Balbuena, X. Li, Lithium-pretreated hard carbon as high-performance sodium-ion battery anodes, Adv. Energy Mater. 8 (2018) 1–10, https://doi.org/10.1002/aenm.201801441.
[133] X. Liu, Y. Tan, T. Liu, W. Wang, C. Li, J. Lu, Y. Sun, A simple electrode-level chemical presodiation route by solution spraying to improve the energy density of sodium-ion batteries, Adv. Funct. Mater. 29 (2019) 1903795, https://doi.org/10.1002/adfm.201903795.
[134] M. Liu, J. Zhang, S. Guo, B. Wang, Y. Shen, X. Ai, H. Yang, J. Qian, Chemically presodiated hard carbon anodes with enhanced initial coulombic efficiencies for high-energy sodium ion batteries, ACS Appl. Mater. Interfaces. 12 (2020) 17620–17627, https://doi.org/10.1021/acsami.0c02230.
[135] K. Nuilek, W. Wongwiriyapan, V. Sattayarut, A. Simon, D. Koncz-Horváth, T. Ferenczi, F. Kristály, P. Baumli, Comparison of acid exfoliators in carbon nanosheets synthesis from stinging nettle (Urtica dioica) for electrochemical applications, Sci. Rep. 10 (2020) 1–12, https://doi.org/10.1038/s41598-020-74286-4.
[136] M. Genovese, J. Jiang, K. Lian, N. Holm, High capacitive performance of exfoliated biochar nanosheets from biomass waste corn cob, J. Mater. Chem. A. 3 (2015) 2903–2913, https://doi.org/10.1039/c4ta06110a.
[137] Z. Li, C. Bommier, Z. Sen Chong, Z. Jian, T.W. Surta, X. Wang, Z. Xing, J. C. Neuefeind, W.F. Stickle, M. Dolgos, P.A. Greaney, X. Ji, Mechanism of Na-Ion storage in hard carbon anodes revealed by heteroatom doping, Adv. Energy Mater. 7 (2017) 1–10, https://doi.org/10.1002/aenm.201602894.
[138] F. Wu, L. Liu, Y. Yuan, Y. Li, Y. Bai, T. Li, J. Lu, C. Wu, Expanding interlayer spacing of hard carbon by Natural K+ Doping to Boost Na-Ion storage, ACS Appl. Mater. Interfaces 10 (2018) 27030–27038, https://doi.org/10.1021/acsami.8b08380.
[139] L. Han, Z. Li, F. Yang, Z. Xiao, Y. Yu, G. Ning, X. Jia, Enhancing capacitive storage of carbonaceous anode by surface doping and structural modulation for high-performance sodium-ion battery, Powder Technol. 382 (2021) 541–549, https://doi.org/10.1016/j.powtec.2021.01.020.
[140] H. Wang, T. Maiyalagan, X. Wang, Review on recent progress in nitrogen-doped graphene: synthesis, characterization, and its potential applications, ACS Catal. 2 (2012) 781–794, https://doi.org/10.1021/cs200652y.
[141] K.C. Wasalathilake, G.A. Ayoko, C. Yan, Effects of heteroatom doping on the performance of graphene in sodium-ion batteries: a density functional theory investigation, Carbon N. Y. 140 (2018) 276–285, https://doi.org/10.1016/j.carbon.2018.08.071.
[142] L. Zhao, H. Yang, F. He, Y. Yao, R. Xu, L. Wang, L. He, H. Zhang, S. Li, F. Huang, Biomimetic N-doped sea-urchin-structured porous carbon for the anode material of high-energy-density potassium-ion batteries, Electrochim. Acta 388 (2021), 138565, https://doi.org/10.1016/j.electacta.2021.138565.
[143] H. Wang, W. Yu, N. Mao, J. Shi, W. Liu, Effect of surface modification on high-surface-area carbon nanosheets anode in sodium ion battery, Microporous Mesoporous Mater. 227 (2016) 1–8, https://doi.org/10.1016/j.micromeso.2016.02.003.
[144] M. Khan, N. Ahmad, K. Lu, Z. Sun, C. Wei, X. Zheng, R. Yang, Nitrogen-doped carbon derived from onion waste as anode material for high performance sodium-ion battery, Solid State Ionics 346 (2020), 115223, https://doi.org/10.1016/j.ssi.2020.115223.
[145] L.A. Romero-Cano, H. García-Rosero, F. Carrasco-Marín, A.F. Pérez-Cadenas, L. V. González-Gutiérrez, A.I. Zárate-Guzmán, G. Ramos-Sánchez, Surface functionalization to abate the irreversible capacity of hard carbons derived from grapefruit peels for sodium-ion batteries, Electrochim. Acta 326 (2019) 1–12, https://doi.org/10.1016/j.electacta.2019.134973.
[146] R.R. Gaddam, A.H. Farokh Niaei, M. Hankel, D.J. Searles, N.A. Kumar, X.S. Zhao, Capacitance-enhanced sodium-ion storage in nitrogen-rich hard carbon, J. Mater. Chem. A. 5 (2017) 22186–22192, https://doi.org/10.1039/c7ta06754b.
[147] Q. Jin, W. Li, K. Wang, P. Feng, H. Li, T. Gu, M. Zhou, W. Wang, S. Cheng, K. Jiang, Experimental design and theoretical calculation for sulfur-doped carbon nanofibers as a high performance sodium-ion battery anode, J. Mater. Chem. A. 7 (2019) 10239–10245, https://doi.org/10.1039/c9ta02107h.
[148] W. Li, M. Zhou, H. Li, K. Wang, S. Cheng, K. Jiang, A high performance sulfur-doped disordered carbon anode for sodium ion batteries, Energy Environ. Sci. 8 (2015) 2916–2921, https://doi.org/10.1039/c5ee01985k.
[149] G. Zhao, G. Zou, H. Hou, P. Ge, X. Cao, X. Ji, Sulfur-doped carbon employing biomass-activated carbon as a carrier with enhanced sodium storage behavior, J. Mater. Chem. A. 5 (2017) 24353–24360, https://doi.org/10.1039/c7ta07860a.
[150] Y. Qiao, R. Han, Y. Pang, Z. Lu, J. Zhao, X. Cheng, H. Zhang, Z. Yang, S. Yang, Y. Liu, 3D well-ordered porous phosphorus doped carbon as an anode for sodium storage: structure design, experimental and computational insights, J. Mater. Chem. A. 7 (2019) 11400–11407, https://doi.org/10.1039/c9ta02268f.
[151] H.M. Wang, H.X. Wang, Y. Chen, Y.J. Liu, J.X. Zhao, Q.H. Cai, X.Z. Wang, Phosphorus-doped graphene and (8, 0) carbon nanotube: structural, electronic, magnetic properties, and chemical reactivity, Appl. Surf. Sci. 273 (2013) 302–309, https://doi.org/10.1016/j.apsusc.2013.02.035.
[152] S. Huang, Y. Lv, W. Wen, T. Xue, P. Jia, J. Wang, J. Zhang, Y. Zhao, Three-dimensional hierarchical porous hard carbon for excellent sodium/potassium storage and mechanism investigation, Mater. Today Energy 20 (2021), 100673, https://doi.org/10.1016/j.mtener.2021.100673.
[153] Y. Zhu, Y. Huang, C. Chen, M. Wang, P. Liu, Phosphorus-doped porous biomass carbon with ultra-stable performance in sodium storage and lithium storage, Electrochim. Acta 321 (2019), 134698, https://doi.org/10.1016/j.electacta.2019.134698.
[154] L.H. Yao, M.S. Cao, H.J. Yang, X.J. Liu, X.Y. Fang, J. Yuan, Adsorption of Na on intrinsic, B-doped, N-doped and vacancy graphenes: a first-principles study, Comput. Mater. Sci. 85 (2014) 179–185, https://doi.org/10.1016/j.commatsci.2013.12.052.
[155] Y. Wang, C. Wang, Y. Wang, H. Liu, Z. Huang, Boric acid assisted reduction of graphene oxide: a promising material for sodium-ion batteries, ACS Appl. Mater. Interfaces 8 (2016) 18860–18866, https://doi.org/10.1021/acsami.6b04774.
[156] N.P. Stadie, E. Billeter, L. Piveteau, K.V. Kravchyk, M. Döbeli, M.V. Kovalenko, Direct synthesis of bulk boron-doped graphitic carbon, Chem. Mater. 29 (2017) 3211–3218, https://doi.org/10.1021/acs.chemmater.7b00376.
[157] Y. Zhang, L. Chen, Y. Meng, X. Li, Y. Guo, D. Xiao, Sodium storage in fluorine-rich mesoporous carbon fabricated by low-temperature carbonization of polyvinylidene fluoride with a silica template, RSC Adv. 6 (2016) 110850–110857, https://doi.org/10.1039/C6RA24386J.
[158] M.J. Jung, E. Jeong, S. Kim, S.I. Lee, J.S. Yoo, Y.S. Lee, Fluorination effect of activated carbon electrodes on the electrochemical performance of electric double layer capacitors, J. Fluor. Chem. 132 (2011) 1127–1133, https://doi.org/10.1016/j.jfluchem.2011.06.046.

[159] M.H. Kim, J.H. Yang, Y.M. Kang, S.M. Park, J.T. Han, K.B. Kim, K.C. Roh, Fluorinated activated carbon with superb kinetics for the supercapacitor application in nonaqueous electrolyte, Colloids Surfaces A Physicochem. Eng. Asp. 443 (2014) 535–539, https://doi.org/10.1016/j.colsurfa.2013.12.020.
[160] D. Qin, Z. Liu, Y. Zhao, G. Xu, F. Zhang, X. Zhang, A sustainable route from corn stalks to N, P-dual doping carbon sheets toward high performance sodium-ion batteries anode, Carbon N. Y. 130 (2018) 664–671, https://doi.org/10.1016/j.carbon.2018.01.007.
[161] Q. Jin, K. Wang, P. Feng, Z. Zhang, S. Cheng, K. Jiang, Surface-dominated storage of heteroatoms-doping hard carbon for sodium-ion batteries, Energy Storage Mater. 27 (2020) 43–50, https://doi.org/10.1016/j.ensm.2020.01.014.
[162] W. Song, J. Kan, H. Wang, X. Zhao, Y. Zheng, H. Zhang, L. Tao, M. Huang, W. Liu, J. Shi, Nitrogen and Sulfur Co-doped Mesoporous Carbon for Sodium Ion Batteries, ACS Appl. Nano Mater. 2 (2019) 5643–5654, https://doi.org/10.1021/acsanm.9b01178.
[163] Z. Pei, Q. Meng, L. Wei, J. Fan, Y. Chen, C. Zhi, Toward efficient and high rate sodium-ion storage: a new insight from dopant-defect interplay in textured carbon anode materials, Energy Storage Mater. 28 (2020) 55–63, https://doi.org/10.1016/j.ensm.2020.02.033.
[164] S. Ikram, S. Dsoke, A. Sarapulova, M. Müller, U.A. Rana, H.M. Siddiqi, Investigation of N and S Co-doped porous carbon for sodium-ion battery, synthesized by using ammonium sulphate for simultaneous activation and heteroatom doping, J. Electrochem. Soc. 167 (2020), 100531, https://doi.org/10.1149/1945-7111/ab9a01.
[165] H. Wan, X. Shen, H. Jiang, C. Zhang, K. Jiang, T. Chen, L. Shi, L. Dong, C. He, Y. Xu, J. Li, Y. Chen, Biomass-derived N/S dual-doped porous hard-carbon as high-capacity anodes for lithium/sodium ions batteries, Energy 231 (2021), 121102, https://doi.org/10.1016/j.energy.2021.121102.
[166] N. Shaji, C.W. Ho, M. Nanthagopal, P. Santhoshkumar, G.S. Sim, C.W. Lee, Biowaste-derived heteroatoms-doped carbon for sustainable sodium-ion storage, J. Alloys Compd. 872 (2021), 159670, https://doi.org/10.1016/j.jallcom.2021.159670.
[167] C. Yang, J. Xiong, X. Ou, C.F. Wu, X. Xiong, J.H. Wang, K. Huang, M. Liu, A renewable natural cotton derived and nitrogen/sulfur co-doped carbon as a high-performance sodium ion battery anode, Mater. Today Energy 8 (2018) 37–44, https://doi.org/10.1016/j.mtener.2018.02.001.
[168] C. Nita, J. Fullenwarth, L. Monconduit, L. Vidal, C., Matei Ghimbeu, Influence of carbon characteristics on Sb/carbon nanocomposites formation and performances in Na-ion batteries, Mater. Today Energy 13 (2019) 221–232, https://doi.org/10.1016/j.mtener.2019.05.009.
[169] C. Luo, Y. Xu, Y. Zhu, Y. Liu, S. Zheng, Y. Liu, A. Langrock, C. Wang, Selenium@Mesoporous carbon composite with superior lithium and sodium storage capacity, ACS Nano. 7 (2013) 8003–8010, https://doi.org/10.1021/nn403108w.
[170] M. Aydin, E. Demir, B. Unal, B. Dursun, A.S. Ahsen, R. Demir-Cakan, Chitosan derived N-doped carbon coated SnO2 nanocomposite anodes for Na-ion batteries, Solid State Ionics 341 (2019), 115035, https://doi.org/10.1016/j.ssi.2019.115035.
[171] H. Sun, J. Wang, W. Li, F. Yuan, Q. Wang, D. Zhang, B. Wang, Y.A. Wu, Spanish-dagger shaped CoP blooms decorated N-doped carbon branch anode for high-performance lithium and sodium storage, Electrochim. Acta 388 (2021), 138628, https://doi.org/10.1016/j.electacta.2021.138628.
[172] Y. Yin, Y. Zhang, N. Liu, B. Sun, N. Zhang, Biomass-derived P/N-Co-doped carbon nanosheets encapsulate Cu3P nanoparticles as high-performance anode materials for sodium-ion batteries, Front. Chem. 8 (2020) 1–8, https://doi.org/10.3389/fchem.2020.00316.
[173] G.X. Pan, F. Cao, D. Xie, Y.J. Zhang, X.H. Xia, Nickel nanoparticles activated highly porous carbon for excellent sodium storage, Electrochim. Acta 292 (2018) 935–941, https://doi.org/10.1016/j.electacta.2018.10.014.
[174] K. Chen, G. Li, Y. Wang, W. Chen, L. Mi, High loading FeS_2 nanoparticles anchored on biomass-derived carbon tube as low cost and long cycle anode for sodium-ion batteries, Green, Energy Environ. 5 (2020) 50–58, https://doi.org/10.1016/j.gee.2019.11.001.
[175] C. Su, Q. Ru, Y. Gao, Z. Shi, M. Zheng, F. Chen, F. Chi-Chung Ling, L.i. Wei, Biowaste-sustained $MoSe_2$ composite as an efficient anode for sodium/potassium storage applications, J. Alloys Compd. 850 (2021) 156770.
[176] W. Tian, L. Wang, K. Huo, X. He, Red phosphorus filled biomass carbon as high-capacity and long-life anode for sodium-ion batteries, J. Power Sources. 430 (2019) 60–66, https://doi.org/10.1016/j.jpowsour.2019.04.086.
[177] Y. Shao, J. Xiao, W. Wang, M. Engelhard, X. Chen, Z. Nie, M. Gu, L.V. Saraf, G. Exarhos, J.G. Zhang, J. Liu, Surface-driven sodium ion energy storage in nanocellular carbon foams, Nano Lett. 13 (2013) 3909–3914, https://doi.org/10.1021/nl401995a.
[178] K. Chayambuka, G. Mulder, D.L. Danilov, P.H.L. Notten, From Li-Ion batteries toward Na-Ion chemistries: challenges and opportunities, Adv. Energy Mater. 10 (38) (2020) 2001310.
[179] A. Bauer, J. Song, S. Vail, W. Pan, J. Barker, Y. Lu, The scale-up and commercialization of nonaqueous Na-Ion battery technologies, Adv. Energy Mater. 8 (2018) 1–13, https://doi.org/10.1002/aenm.201702869.